

INTERSTELLAR DEUTERIUM, NITROGEN, AND OXYGEN ABUNDANCES TOWARD GD 246, WD 2331–475, HZ 21, AND LANNING 23: RESULTS FROM THE *FUSE* MISSION¹

CRISTINA M. OLIVEIRA,² GUILLAUME HÉBRARD,³ J. CHRISTOPHER HOWK,^{2,4} JEFFREY W. KRUK,²
PIERRE CHAYER,^{2,5} AND H. WARREN MOOS²

Received 2002 October 31; accepted 2002 December 13

ABSTRACT

The interstellar abundances of D I, N I, and O I in the local ISM are studied using high-resolution spectra of four hot white dwarfs. The spectra of GD 246, WD 2331–475, HZ 21, and Lan 23 were obtained with the *Far Ultraviolet Spectroscopic Explorer (FUSE)* in the wavelength range 905–1187 Å. The line of sight to GD 246 probes the Local Interstellar Cloud and at least one other H I cloud inside the Local Bubble, which contains most of the gas seen along this line of sight. The column densities of H I, C II*, S II, and Si II are measured using archival *Hubble Space Telescope* STIS echelle-mode observations. The H I column density is determined by fitting the strong damping wings of interstellar Ly α and using a model atmosphere to account for the stellar continuum. The sight line-averaged ratios for GD 246 are D I/H I = $1.51^{+0.39}_{-0.33} \times 10^{-5}$, O I/H I = $3.63^{+0.77}_{-0.67} \times 10^{-4}$, and D I/O I = $4.17^{+1.20}_{-1.00} \times 10^{-2}$ (uncertainties are 2 σ). This line of sight provides the fourth reliable *FUSE* measurement of the Local Bubble D/H ratio. For the WD 2331–475 line of sight, we find sight line-averaged ratios D I/O I = $5.13^{+2.20}_{-1.69} \times 10^{-2}$ and D I/N I = $4.57^{+1.88}_{-1.45} \times 10^{-1}$. Toward HZ 21 the sight line-averaged ratios are D I/O I = $4.57^{+2.22}_{-1.63} \times 10^{-2}$ and D I/N I = $4.27^{+1.96}_{-1.44} \times 10^{-1}$. In the higher column density sight line to Lan 23, the sight line-averaged ratios are D I/O I = $3.24^{+3.27}_{-2.06} \times 10^{-2}$ and D I/N I = $3.16^{+1.56}_{-1.23} \times 10^{-1}$. Molecular hydrogen, corresponding to rotational levels $J \leq 3$, is clearly seen along this line of sight. No reliable H I measurements are available for WD 2331–475, HZ 21, or Lan 23. We combine the different abundance ratios computed here with previous published values to produce revised *FUSE* abundance ratios for D I/H I, O I/H I, N I/H I, D I/N I, D I/O I, and O I/N I.

Subject headings: ISM: abundances — ISM: evolution —

stars: individual (GD 246, HZ 21, Lanning 23, WD 2331–475) — ultraviolet: ISM

1. INTRODUCTION

The present-day abundance ratio of deuterium to hydrogen places important constraints on big bang nucleosynthesis (BBN) and the chemical evolution of galaxies. Since it is believed that deuterium is only produced in appreciable amounts in primordial BBN and destroyed in stellar interiors, the measurement of D I/H I in the interstellar medium (ISM) places a lower limit on the primordial abundance of deuterium. By comparing the ISM abundance of deuterium to its abundance in high-redshift intergalactic gas, we should be able to understand better the effects of astration and chemical evolution of galaxies. Measurements of the D/H ratio in intervening clouds of gas seen toward distant quasars have yielded a range of values $D/H = (1.65\text{--}4.0) \times 10^{-5}$ (O’Meara et al. 2001; Pettini & Bowen 2001; Levshakov et al. 2002 and references therein). Measurements of D/H in the local ISM have been made with *Copernicus* (see, e.g., Rogerson & York 1973), the *Hubble Space Telescope (HST)* (see, e.g., Linsky et al. 1995), *IMAPS* (Jenkins et al. 1999; Sonneborn et al. 2000), and

more recently the *Far Ultraviolet Spectroscopic Explorer (FUSE)*; Moos et al. 2002 and references therein). A nearly constant ratio of $D/H = (1.5 \pm 0.1) \times 10^{-5}$ (1 σ on the mean) has been obtained in the Local Interstellar Cloud (LIC) by Linsky (1998); recent measurements inside the Local Bubble (Moos et al. 2002) appear to be consistent with a single value for D/H in the Local Bubble. Other measurements (Laurent, Vidal-Madjar, & York 1979; York 1983; Hébrard et al. 1999; Jenkins et al. 1999; Sonneborn et al. 2000) suggest variations of the interstellar D/H ratio beyond the Local Bubble, at the distance of a few hundred parsecs.

Until the *FUSE* was launched (1999 June 24), only the UV spectrographs on board *HST* could be used for systematic studies of the deuterium abundance in the ISM. Since only the Ly α transitions of H I and D I are observable in the *HST* bandpass, such studies were restricted to low column density sight lines, so that D I was neither completely obscured by the adjacent H I Ly α nor heavily saturated. With *FUSE*, we now have access to the complete Lyman series of deuterium (except Ly α), which allows the study of a larger range of environments and provides tighter constraints on the abundance of D I, compared to studies using only Ly α . In addition, the numerous lines of N I, O I, and Fe II in the *FUSE* bandpass can be used to trace the metallicity and dust content of the absorbing gas.

In this work we present the first measurements of deuterium absorption toward the white dwarfs GD 246, WD 2331–475, HZ 21, and Lan 23. Table 1 summarizes the stellar parameters. This study adds four more sight lines to the seven sight line studies that constitute the first set of *FUSE* deuterium measurements (see overview paper by Moos et al.

¹ Based on observations made with the NASA-CNES-CSA *Far Ultraviolet Spectroscopic Explorer (FUSE)*, which is operated for NASA by Johns Hopkins University under NASA contract NAS 5-32985.

² Department of Physics and Astronomy, Johns Hopkins University, Baltimore, MD 21218.

³ Institut d’Astrophysique de Paris, 98bis boulevard Arago, F-75014 Paris, France.

⁴ Current address: Center for Astrophysics and Space Sciences, University of California at San Diego, C-0424, La Jolla, CA 92093.

⁵ Department of Physics and Astronomy, University of Victoria, P.O. Box 3055, Victoria, BC V8W 3P6, Canada.

TABLE 1
STELLAR PROPERTIES

Star	WD Number	Spectral Type	l (deg)	b (deg)	d^a (pc)	V (mag)	T_{eff}^b (K)	$\log g^b$ (cm s^{-2})	Reference
GD 246	2309+105	DA	87.25	-45.11	79 ± 24	13.09	$53,088 \pm 968$	7.85 ± 0.07	1
WD 2331-475	2331-475	DA	334.85	-64.81	82 ± 25	13.1	$51,800 \pm 800$	7.79 ± 0.07	2
HZ 21	1211+332	DO	175.04	+80.03	115 ± 35	14.22	$53,000 \pm 2650$	7.8 ± 0.3	3
Lan 23	2247+583	DA	107.64	-0.64	122 ± 37	14.26	$59,360 \pm 800$	7.84 ± 0.05	2

^a All distances are photometric; 30% error adopted.

^b The uncertainties quoted are 1σ .

REFERENCES.—(1) Napiwotzki, Green, & Saffer 1999; (2) Vennes et al. 1997; (3) Dreizler & Werner 1996.

2002 and references therein). This paper is organized as follows. The observations and data processing are presented in § 2; the analysis methodology is described in § 3. The GD 246 line-of-sight analysis is presented in § 4. The WD 2331-475, HZ 21, and Lan 23 lines of sight are analyzed in § 5, and systematic effects are discussed in § 6. We discuss the results in § 7.

2. OBSERVATIONS AND DATA PROCESSING

2.1. *FUSE* Observations

The *FUSE* observatory consists of four co-aligned prime-focus telescopes and Rowland circle spectrographs that produce spectra over the wavelength range 905–1187 Å with a spectral resolution of ~ 15 –20 km s^{-1} (wavelength-dependent) for point sources. Two of the optical channels employ SiC coatings, providing reflectivity in the wavelength range ~ 905 –1000 Å, while the other two have LiF coatings for maximum sensitivity above 1000 Å. Dispersed light is focused onto two photon-counting microchannel plate detectors. With this arrangement of optical channels (LiF 1, LiF 2, SiC 1, and SiC 2) and detector segments (1A, 1B, 2A, and 2B) the *FUSE* instrument has eight segments: LiF 1A, LiF 1B, LiF 2A, LiF 2B, SiC 1A, SiC 1B, SiC 2A, and SiC 2B. Four channels cover the wavelength range 1000–1080 Å, while two channels each cover the ranges 900–1000 and 1080–1180 Å. The *FUSE* mission, its

planning, and its on-orbit performance are discussed by Moos et al. (2000) and Sahnou et al. (2000).

Table 2 summarizes the *FUSE* observations of the four white dwarfs studied in this work. The *FUSE* spectrum of the hot DA white dwarf GD 246 is shown in Figure 1. Observations were obtained through both the large (LWRS; $30'' \times 30''$) and the medium-sized apertures (MDRS; $4'' \times 20''$) in histogram mode (HIST, in which a two-dimensional spectral image is accumulated and down-linked). The spectrum of WD 2331-475 is shown in Figure 2. Two observations were obtained through the LWRS aperture and one through the MDRS aperture. All of them were obtained in HIST mode. During one of the LWRS observations (P1044202), one detector (side 2) was not available, resulting in the loss of data from the LiF 2A, LiF 2B, SiC 2A, and SiC 2B channels. The spectrum of HZ 21 is shown in Figure 3. The data were obtained through the LWRS and MDRS apertures, in time-tag mode (TTAG, in which the position and arrival time of each photon are recorded). The *FUSE* spectrum of the hot DA white dwarf Lan 23 is displayed in Figure 4. The data were obtained through the LWRS aperture in TTAG mode.

For the four stars the two-dimensional *FUSE* spectra are reduced using the CalFUSE pipeline (version 2.0.5; V. Dixon, J. Kruk, & E. Murphy 2003, in preparation⁶). The

⁶ The CalFUSE pipeline reference guide is available at http://fuse.pha.jhu.edu/analysis/pipeline_reference.html.

TABLE 2
LOG OF *FUSE* OBSERVATIONS

Star	Program ID	Date	Aperture ^a	Exposures	Exposure Time (ks)	Mode ^b	S/N ^c
GD 246	M1010602	1999 Dec 9	MDRS	2	1.2	HIST	4.6
	M1010604	1999 Dec 10	LWRS	7	3.4	HIST	6.4
	P1044101	2000 Jul 19	LWRS	28	14.8	HIST	8.6
	M1010601	2000 Nov 12	LWRS	3	1.6	HIST	5.2
	P2042401	2001 Jul 14	MDRS	51	24.6	HIST	8.3
WD 2331-475	P1044202	1999 Nov 8	LWRS	29	20.2	HIST	8.2
	P1044201	2000 Jun 23	LWRS	20	19.4	HIST	8.4
	P1044203	2002 Jul 27	MDRS	72	32.1	HIST	8.3
HZ 21	M1080201	2000 May 10	LWRS	5	4.9	TTAG	4.4
	P2040801	2001 Jan 27	LWRS	4	12.4	TTAG	5.2
	P2040802	2001 Feb 6	MDRS	25	16.7	TTAG	5.5
Lan 23	P2510101	2001 Jul 19	LWRS	8	20.4	TTAG	4.7

^a See text for definition of aperture.

^b See text for definition of observing mode.

^c Signal-to-noise ratios, per detector pixel, measured in the LiF 1A segment between 1000 and 1005 Å for all stars except Lan 23, for which we use the range 995–1000 Å.

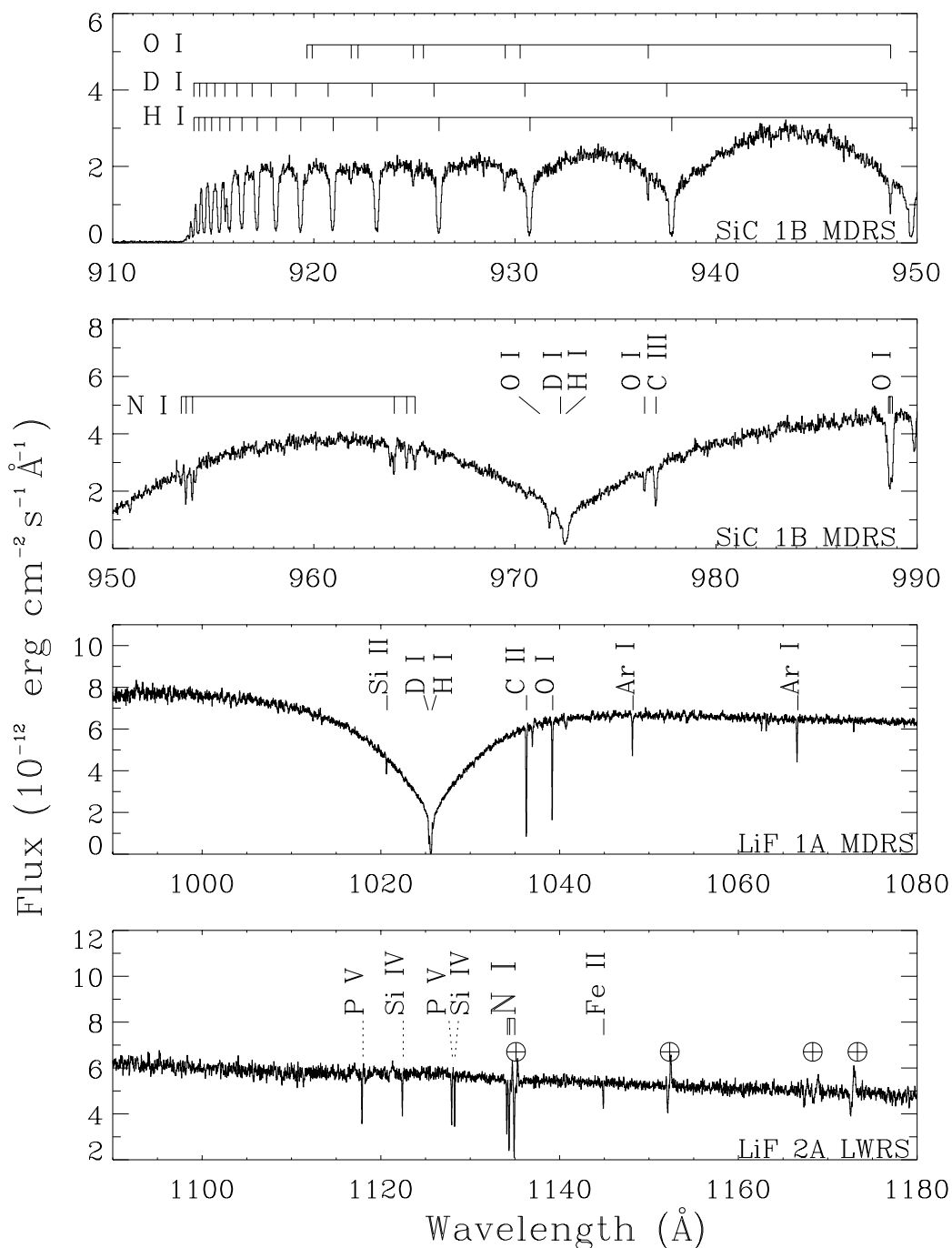


FIG. 1.—*FUSE* spectra of GD 246, with identification of interstellar lines. An annotation on each panel indicates which channels are displayed and if the data were obtained through the LWRS or MDRS apertures. Photospheric lines are marked with dotted lines, and geocoronal emission is annotated with crossed circles. Ar I λ 1066 is blended with stellar Si IV. Data are binned by 4 for display purposes only.

processing includes data screening for low-quality or unreliable data, thermal drift correction, geometric distortion correction, heliocentric velocity correction, dead-time correction, wavelength calibration, detection and removal of event bursts, background subtraction, and astigmatism correction. The spectra are aligned by cross-correlating the individual exposures over a short wavelength range that contains prominent spectral features and then co-added by weighting each exposure by its exposure time. All the spectra are binned to 3 pixel samples, or 20 mÅ, for analysis (the

line-spread function [LSF] is about 11 pixels, or ~ 70 mÅ, wide).

2.2. *STIS* Observations of GD 246 and Data Processing

Two *HST/STIS* observations of GD 246 that include H I Ly α are available at the Multimission Archive at the Space Telescope Science Institute, one each using the E140H and E140M gratings.

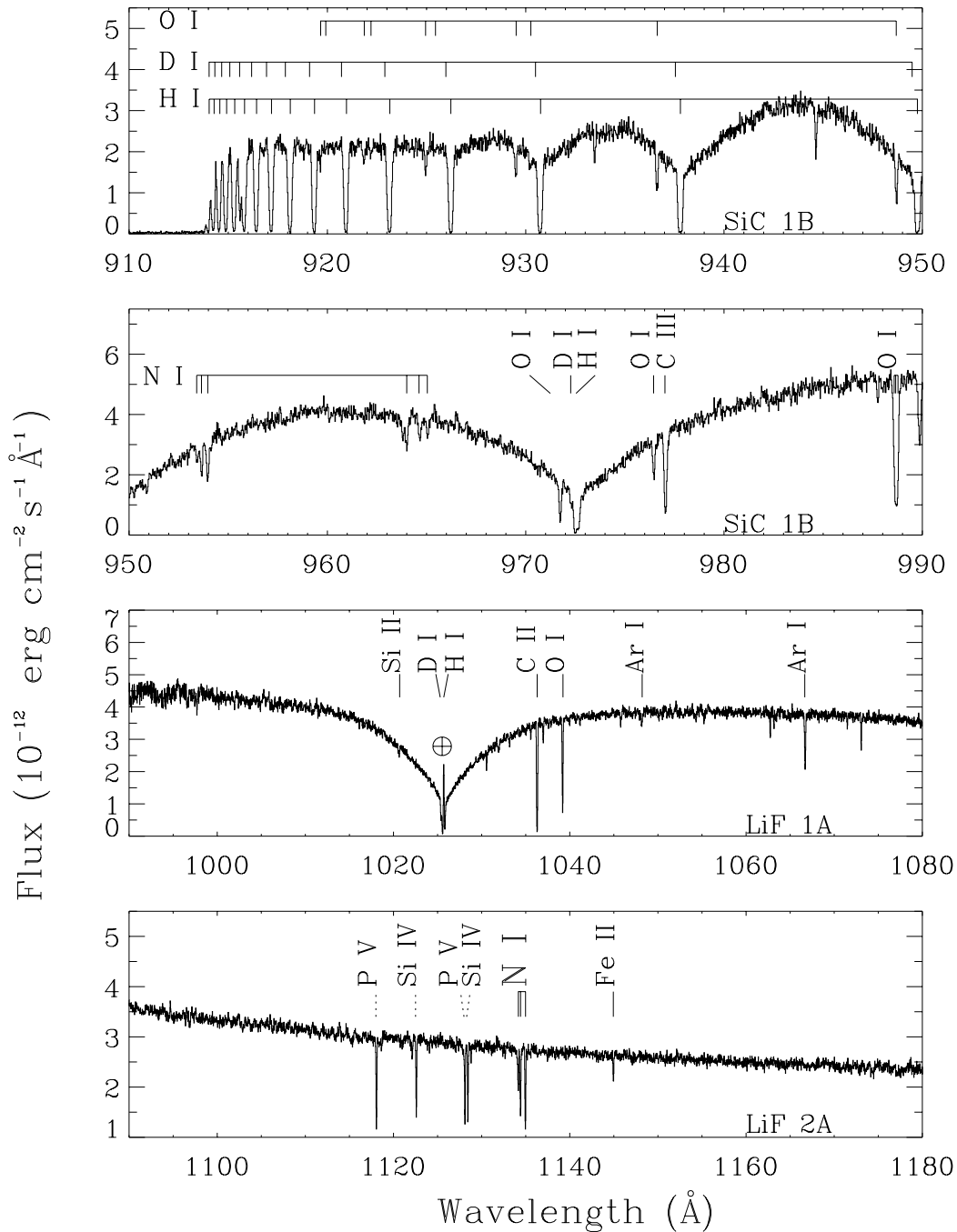


FIG. 2.—Same as Fig. 1, but for WD 2331–475. Data presented here are from the MDRS observation P1044203.

Although the E140H grating has better resolution than the E140M grating, it also suffers from more complications in the $\text{Ly}\alpha$ region. $\text{Ly}\alpha$ spans more orders in the E140H grating, and the relative flux calibration of adjacent orders is not as good as the one for the E140M grating. Because the saturated H I $\text{Ly}\alpha$ line is so broad, the higher resolution of the E140H grating is not required. Therefore, we make use of the E140M data for deriving the H I column density. We use the E140H data to study the abundance of metals, such as C II*, Si II, and S II, and to determine the velocity structure of the gas along the line of sight.

The STIS echelle-mode observations of GD 246 are summarized in Table 3. The E140M (S/N ~ 15 , FWHM = 1.3

pixels) and E140H (S/N ~ 10 –25, FWHM = 1.2 pixels) data are reduced using the standard STSDAS pipeline within IRAF. The CALSTIS pipeline (version 2.3) is used to produce the two-dimensional spectrum of the FUV-MAMA, and then the scattered light removal is performed using different algorithms for the different echelle gratings. For the E140M data, the Lindler & Bowers (2000) algorithm is used to estimate and remove the scattered light from the data in the pipeline procedure. After the spectrum is extracted, two echelle spectral orders in the regions adjacent to $\text{Ly}\alpha$ are combined using a weighted averaging scheme in which the orders overlap. For the E140H data, the scattered light is removed with the procedure of Howk & Sembach (2000).

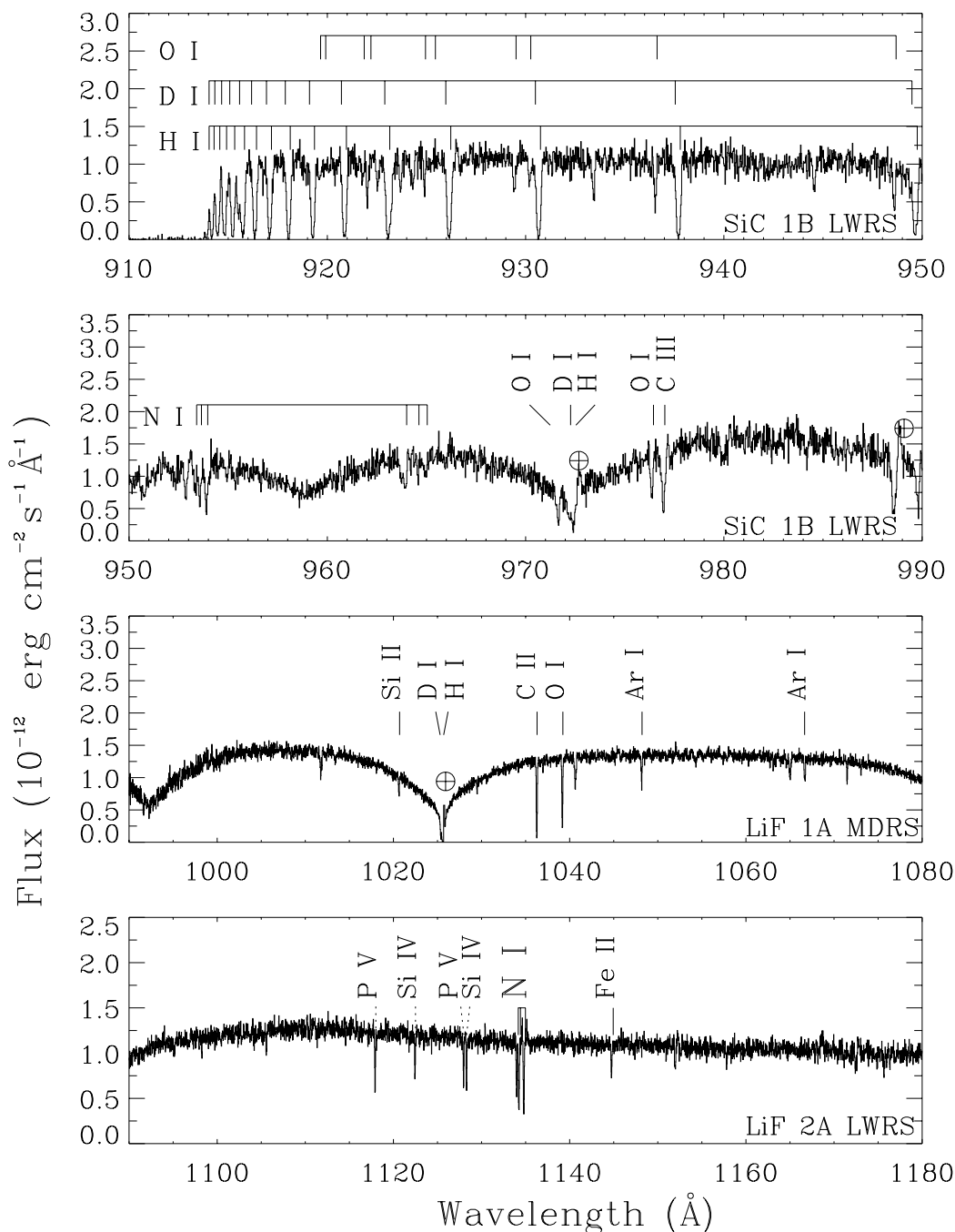


FIG. 3.—Same as Fig. 1, but for HZ 21

3. ANALYSIS METHODOLOGY

Whenever possible we derive the column densities by more than one method. We use profile-fitting (PF), curve-of-growth (COG), and apparent optical depth (AOD) methods. Table 4 indicates which methods are used for each transition in the four stars. Below we discuss the techniques used in more detail.

3.1. Profile Fitting

We use the PF code “Owens.f” developed by Martin Lemoine and the French *FUSE* team to derive the column densities presented in this study. In this approach each interstellar absorption line is represented by the convolution of a

theoretical Voigt absorption profile with the instrumental LSF, taken to be a single Gaussian in this work. An iterative procedure that minimizes the sum of the squared differences between model profiles and the data is used to determine the most likely column densities N , radial velocities, and velocity dispersions of each component. The stellar continua in the vicinity of the absorption lines being studied are normalized by Chebyshev polynomials of low order. Unsaturated lines from different elements in different spectral regions (designated “windows”) are fitted simultaneously to give a single solution for the temperature, nonthermal velocity, and radial velocity of each cloud (we define as unsaturated those lines for which the absorption profile, before convolution with the instrumental LSF, has a residual intensity in

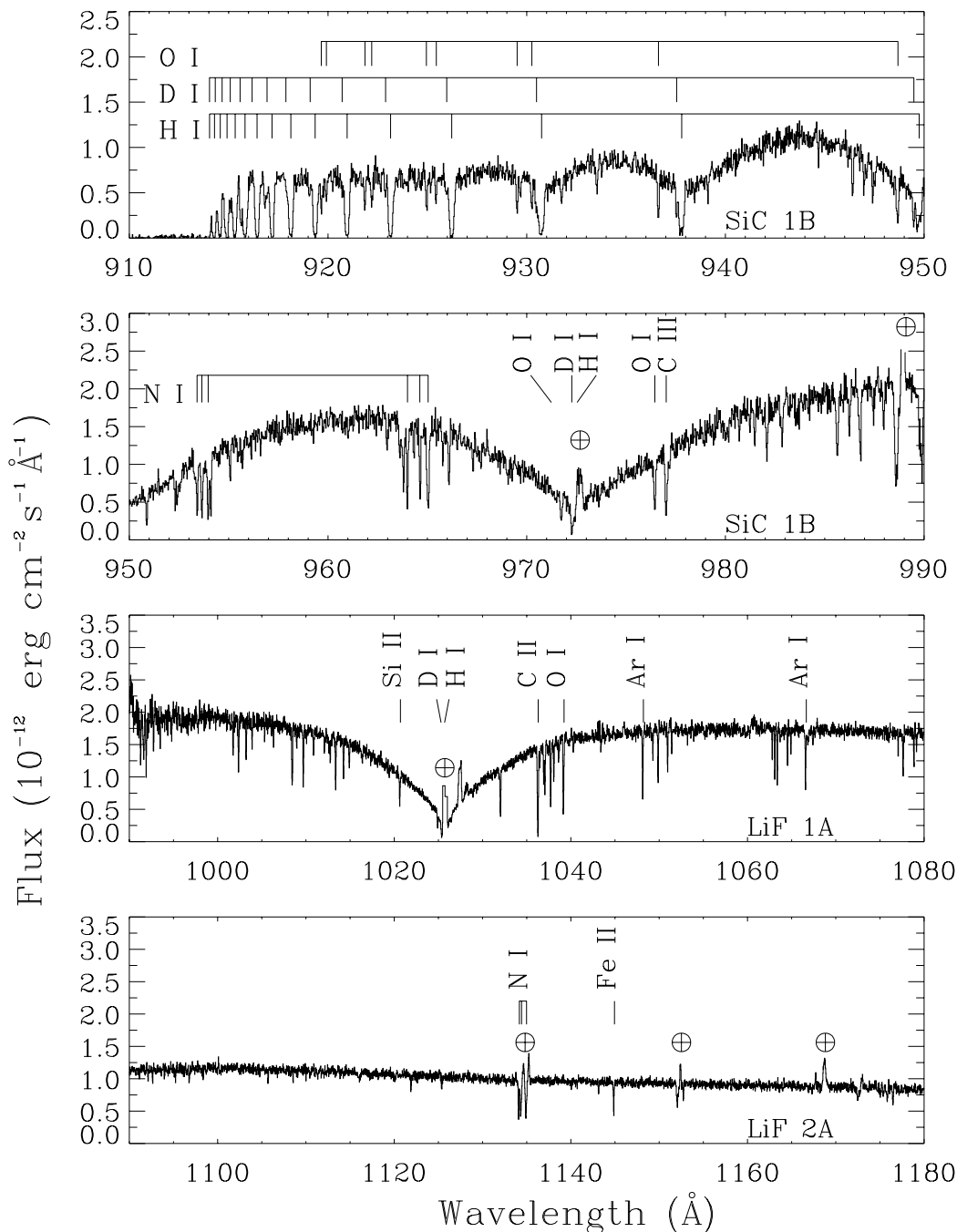


FIG. 4.—Same as Fig. 1, but for Lan 23. Many lines of molecular hydrogen (not marked) are also seen along this line of sight, e.g., in the range 1000–1020 \AA .

the line core larger than 0.1). The software also allows us to use a wavelength-dependent LSF and relative wavelength shifts between different absorption lines as free parameters. These last two features are particularly convenient when fit-

ting *FUSE* data, for which the LSF, while poorly constrained, is known to vary with wavelength. There are also small wavelength shifts between and within channels that are accommodated by this approach. For more on profile

TABLE 3
STIS ECHELLE OBSERVATIONS OF GD 246

Program ID	Date	Grating	Aperture (arcsec)	Exposure Time (s)	Wavelengths Covered (\AA)
O4G102010.....	1998 Nov 20	E140M	0.02×0.06	1699.0	1140–1735
O4G102020.....	1998 Nov 20	E140H	0.02×0.09	2420.0	1170–1372

TABLE 4
 ATOMIC DATA AND ANALYSIS METHODS FOR THE LINES USED IN THE ANALYSES

Species	Wavelength (Å)	$\log f\lambda$	GD 246	WD 2331–475	HZ 21	Lan 23
H I.....	1215.670	2.70	P
D I.....	920.713	0.17	P
	922.899	0.31	P
	925.974	0.47	P	P
	930.495	0.65	P	...	P	P
	937.548	0.86	P	P	P	P
	949.485	1.12	P	P	P	...
	972.272	1.45	P	P
	1025.443	1.91	...	P
C II*.....	1037.018	2.11	P	P, A	A	A
	1335.663	1.23	P
	1335.708	2.23	P
N I.....	952.303	0.25	P
	952.415	0.21	P
	952.523	-0.24	P
	953.415	1.10	...	P, C	P, C	...
	953.655	1.38	...	P, C	P, C	...
	953.9699	1.52	...	P, C
	954.1042	0.81	...	P
	963.990	1.54	...	P	P, C	...
	964.626	0.96	P, C	P, C	P, C	...
	965.041	0.59	P, C	P	P, C	...
	1134.1653	1.69	...	P, C
	1134.4149	1.53	...	P, C
	1134.9803	1.24	...	P, C
	1199.550	2.19	C
	1200.223	2.01	C
	1200.710	1.71	C
N II.....	1083.994	2.10	A	A	A	A
O I.....	919.658	-0.06	P, C	P, C	P, C	...
	919.917	-0.79	P, C	P	P, C	P, A
	921.875	0.04	P, C	P, C
	922.200	-0.65	P	P
	924.950	0.15	P, C	P, C	P, C	...
	925.446	-0.49	P, C	P	P, C	...
	929.5168	0.32	...	P, C
	930.257	-0.30	P, C	P	P, C	...
	936.6295	0.53	...	P, C
	948.6855	0.77	C	C	C	C
	950.885	0.18	P, C
	971.738	1.13	C	C	C	C
	972.142	-0.47	P	P
	974.070	-1.82	P
	976.4481	0.51	...	P, C
	1039.2301	0.98	C	C	C	C
Si II.....	1020.699	1.22	P, C	P, A	P, A	A
	1190.416	2.54	P, C
	1193.230	2.84	P, C
	1304.370	2.08	P, C
P II.....	963.800	3.15	P	P, A	P, A	A
S II.....	1250.584	0.83	P, C
	1253.811	1.14	P, C
	1259.519	1.32	P, C
Ar I.....	1048.220	2.44	P	P, A	P, A	A
Fe II.....	1063.176	1.76	P	...	P, A	P, C
	1121.975	1.36	P, C
	1125.448	1.26	P, C, A
	1144.938	2.08	P	P, A	...	P, C

NOTE.—P, C, and A, denote lines that are analyzed with PF, COG, and AOD, respectively.

fitting with this code, see Hébrard et al. (2002) and Lemoine et al. (2002).

Two of us (C. M. O. and G. H.) performed the analyses for GD 246, WD 2331–475, HZ 21, and Lan 23 independently. In both of the analyses a Gaussian LSF is used. However, in one analysis (PF1) the FWHM of the LSF for each spectral window is allowed to vary independently during the fitting process, while in the other (PF2) it is not allowed to vary. In PF2 there is an initial step in which all LSFs are free parameters of the fit. After a few trial fits, the LSFs for the different windows converge and do not change significantly (these values are close to each other and close to what is known about the *FUSE* LSF). At this point the LSFs are fixed at the newly found values, reducing the number of free parameters, for the remainder of the χ^2 minimization. We find typical LSF values of 8–13 pixels (FWHM 53.6–87.1 mÅ) for the PF1 analysis; for the PF2 analysis we find a range of 9–13 pixels for the LSF (FWHM 60.3–87.1 mÅ). The background levels used for each line are those evaluated at the bottom of the closest Lyman line (see Hébrard et al. 2002). When possible, we compare the different channels and data sets to check for fixed-pattern noise in the regions of the absorption lines used in this study. When there is an inconsistency between channels and/or observations we remove that absorption line from our fit.

The error bars for each estimated column density are computed from an analysis of the χ^2 variation. The column density for which the error bars are being sought is fixed at a series of trial values, and for each trial value we compute the best fit and resulting χ^2 distribution, for which all the other parameters are allowed to vary freely. To define the confidence interval we use the distribution of χ^2 . Scanning the column density in this way, we obtain the value of χ^2 as a function of the column density and derive the 1, 2, 3, 4, 5, 6, and 7 σ confidence levels using the standard $\Delta\chi^2$ method. The 1, 2, 3, 4, 5, 6, and 7 σ error bars are divided by 1, 2, 3, 4, 5, 6, and 7, respectively. The average of these values, multiplied by 2, is then used to produce the final 2 σ uncertainties reported here. For more on the $\Delta\chi^2$ method, see Hébrard et al. (2002) or Lemoine et al. (2002). We adopt the wavelengths and oscillator strengths for molecular hydrogen from Abgrall et al. (1993a, 1993b) and use Morton (1991)

with updates from D. C. Morton (1999, private communication for the other species (see Table 4).

Both analyses produce similar results, and the final values quoted here reflect the combined effort of these analyses. The results for all the four lines of sight are summarized in Table 5 and in § 5.

3.2. Curve of Growth and Apparent Optical Depth

We use the COG and AOD techniques to estimate the column densities of some species as a consistency check of the PF results. Not all species analyzed by PF are suitable for analysis with these two methods. In the cases in which the continuum is difficult to place (such as D I) or there is blending (such as the N I triplets), we do not construct a COG or use the AOD technique. Since in these two techniques each absorption line is studied individually, continuum placement in a “problematic” line is harder than when many different lines of different absorption strengths and different continua are analyzed simultaneously, as is the case for PF. For species with only a small number of transitions available (such as P II and Ar I) we do not construct a COG, but we are able to use the AOD method.

In the COG technique the measured equivalent widths are fitted with a single-component Gaussian COG (Spitzer 1978). In this technique the Doppler parameter, b , and column density, N , are varied so as to minimize the χ^2 between the measured equivalent widths and a model COG. The stellar continuum in the vicinity of each line is estimated using a low-order Legendre polynomial fit to the data. Contributions from Poisson noise, uncorrected high-frequency fixed-pattern noise, uncertainties in the Legendre fit parameters, and systematic uncertainties in the continuum placement and velocity integration range are used to estimate the uncertainties in the measured equivalent widths (see Sembach & Savage 1992 for details on this procedure). We measure the equivalent widths of a particular transition in all segments for which that wavelength is covered. All the measurements from the different segments are compared; those that differ by more than 2 σ are excluded from our analysis (the differences are probably due to fixed-pattern noise).

TABLE 5
ADOPTED COLUMN DENSITIES

Species	GD 246 (cm ⁻²)	WD 2331–475 (cm ⁻²)	HZ 21 (cm ⁻²)	Lan 23 ^a (cm ⁻²)
log $N(\text{H I})$	19.11 ± 0.05	19.89 ^{+0.49} _{-0.08}
log $N(\text{D I})$	14.29 ± 0.09	14.19 ± 0.12	14.40 ± 0.15	15.23 ± 0.13
log $N(\text{C II}^*)$	13.05 ± 0.04	13.24 ± 0.17	12.97 ^{+0.20} _{-0.27}	≥13.65
log $N(\text{N I})$	14.75 ± 0.06	14.53 ± 0.10	14.77 ± 0.08	15.73 ^{+0.13} _{-0.15}
log $N(\text{N II})$	≥13.81	≥14.27	≥14.03	≥13.95
log $N(\text{O I})$	15.67 ± 0.07	15.48 ± 0.11	15.74 ± 0.10	16.72 ^{+0.29} _{-0.38}
log $N(\text{Si II})$	14.07 ^{+0.06} _{-0.04}	13.99 ± 0.20	14.36 ± 0.08	≥14.52
log $N(\text{P II})$	12.29 ± 0.10	12.18 ± 0.20	12.57 ^{+0.12} _{-0.15}	≥12.72
log $N(\text{S II})$	14.34 ± 0.02
log $N(\text{Ar I})$	13.14 ^{+0.13} _{-0.10}	12.77 ± 0.20	13.16 ± 0.05	≥13.50
log $N(\text{Fe II})$	13.30 ± 0.10	13.32 ± 0.10	13.54 ± 0.08	14.03 ± 0.13

NOTE.—Adopted values are the combination of PF1 and PF2 (see text for more on this). All uncertainties are 2 σ .

^a $N(\text{H I})$ from Wolff, Koester, & Lallement 1999. Range quoted includes uncertainty in the photospheric composition of this star (see § 5).

In the AOD technique the column density is determined by directly integrating the apparent column density profile, $N_a(v) = 3.768 \times 10^{14} \tau_a(v) / [f\lambda(\text{\AA})]$, over the velocity range of the absorption profile (see Savage & Sembach 1991). The continuum is placed in the same way as described above in the COG method. This technique only yields the true total column density when the absorption is weak ($\tau \leq 1$) or, if partially saturated, the components of the lines are fully resolved.

All the lines used in PF, COG, and AOD analyses are shown in Table 4, along with $\log f\lambda$ for each transition. For each star, P, C, and A denote transitions that are used in PF, COG, and AOD analyses, respectively. Both the COG and AOD techniques produce results that generally have higher uncertainties, but are accurate enough to use as consistency checks. These checks show that the AOD and COG results are within the 2σ uncertainties of the column densities determined using PF.

4. ANALYSIS OF THE GD 246 LINE OF SIGHT

GD 246 is a hot, hydrogen-rich (DA) white dwarf with effective temperature and gravity $T_{\text{eff}} \sim 53,000$ K and $\log g \sim 7.85$, respectively. The *FUSE* spectra of GD 246 show a smooth stellar continuum against which the interstellar lines are cleanly seen. Apart from the broad stellar Lyman lines, only a few stellar lines are present (Si IV and P IV–V). No molecular hydrogen or O VI lines are detected along this line of sight.

High-resolution STIS echelle spectra of GD 246 show that there are at least two velocity components, separated by ~ 9 km s⁻¹, along this line of sight. These are seen in the N I, S II, and Si II absorption profiles (see Fig. 5). As

discussed in § 7.5, the weaker component likely probes the LIC.

The two PF analyses of this line of sight are different in an additional way. In one of the PF analyses (PF1) of this line of sight we use only *FUSE* data with a variable LSF; in the other PF analysis (PF2) we use both *FUSE* and STIS data with fixed, but different, LSFs for the *FUSE* and STIS spectral windows. Both analyses are described in more detail below.

4.1. Profile Fits

In PF1 we fit a one-component model to D I, C II*, N I, O I, Si II, P II, Ar I, and Fe II, using *FUSE* data only. The FWHM of the LSF is a free parameter of the fit for each spectral window being fitted.

For PF2 we use high-resolution STIS E140H spectra ($R \sim 114,000$) of GD 246, covering the wavelength region 1170–1372 Å, to constrain the velocity structure along the line of sight, as well as to measure the column density of species with no transitions in the *FUSE* bandpass (such as S II). Species that have transitions in the *FUSE* and STIS bandpasses are fitted simultaneously in both data sets. For the STIS data we use a single-Gaussian LSF with an FWHM of 2 pixels for all the spectral windows. In this analysis we fit one absorption component to D I, C II*, N I, O I, Si II, S II, and Fe II, at the best-fit velocity of $v_{\odot} = -9.76$ km s⁻¹. For N I, Si II, and S II we use two components: component 1 at the best-fit velocity of $v_{\odot} = -9.76$ km s⁻¹ and component 2 at the best-fit velocity of $v_{\odot} = -0.63$ km s⁻¹.

The decision to distribute the second set of ions between two components is based on the following arguments. From an independent analysis of the STIS data alone, in which we fitted two components to N I, Si II, and S II, we determined

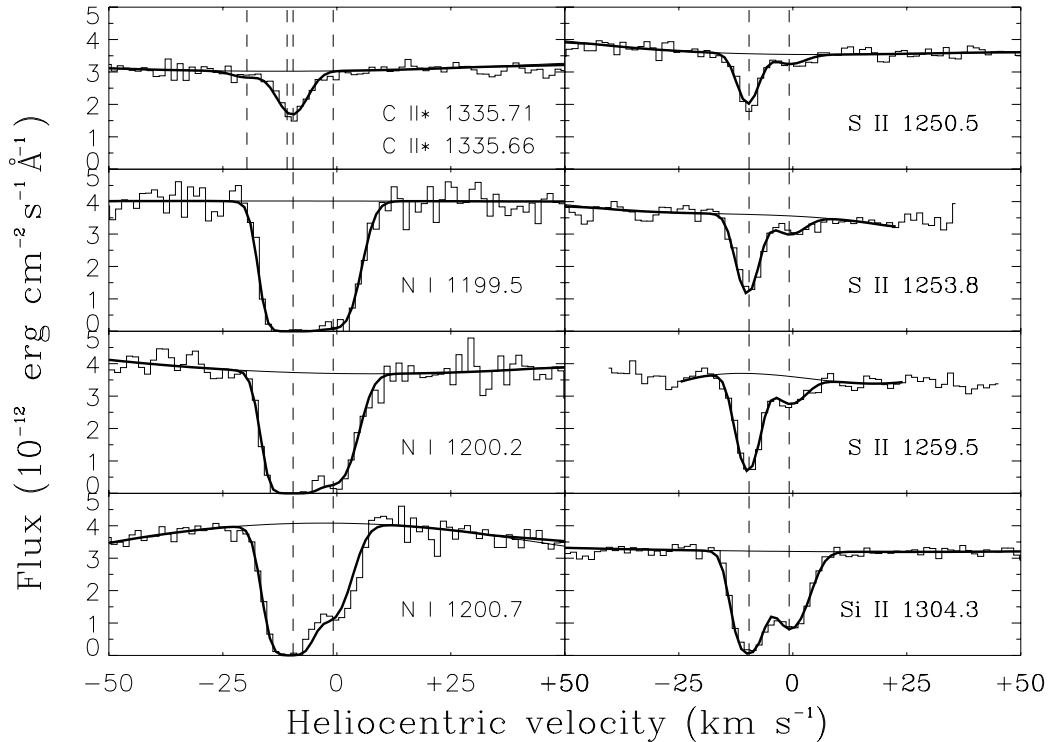


Fig. 5.—STIS echelle spectra of GD 246, showing two absorption components. The two components at $v_{\odot} = -9.8$ and -0.6 km s⁻¹ are marked by vertical lines. The weak component at -0.6 km s⁻¹ is identified with the LIC in § 7.5. The bold line represents the fit to the absorption lines.

that component 1 contains most of the material seen along this line of sight and that the Doppler parameters of the two components are similar. The ratios of column densities of component 1 to component 2 are $N(\text{N I})_1/N(\text{N I})_2 = 5.9$, $N(\text{S II})_1/N(\text{S II})_2 = 4.6$, and $N(\text{Si II})_1/N(\text{Si II})_2 = 2.3$. For species for which there are no STIS data, a velocity separation of $\sim 9 \text{ km s}^{-1}$ between the two components is not enough for profiles at the *FUSE* resolution to produce meaningful results about the relative strength of the two different components. Since the physical parameters of the components seem to be similar, we would expect component 1, the stronger one, to saturate first. However, we chose lines in the *FUSE* data that appear unsaturated so that we did not have to worry about hidden saturation effects that would bias our column density determinations. For these reasons we choose to fit two components for the species for which we have STIS echelle data and one component for the species with no STIS data. In the end, the results of the two different approaches, PF1 and PF2, are consistent at the 2σ level, with most consistent at the 1σ level.

Because of the better resolution and signal-to-noise ratio of the STIS E140H data, we have tighter constraints on the column densities of C II^* , S II , and Si II , in the model in which STIS and *FUSE* data are fitted simultaneously. For this reason the column densities and error bars reported for these species (Table 5) are the ones obtained with PF2. Profile fits for D I (PF2) are presented in Figure 6, and the combined results are presented in Table 5.

4.2. Determination of the H I Column Density toward GD 246

The H I column density along this sight line is determined by fitting the strong damping wings of interstellar $\text{Ly}\alpha$ using a newly computed model atmosphere to account for the stellar continuum. We consider the influence on the $\text{Ly}\alpha$ profile of several stellar models with different effective temperatures and gravities. *HST*/STIS E140M ($\lambda/\Delta\lambda \equiv R \approx 45, 800$) archival data are used in this analysis.

4.2.1. Stellar Model

Several investigators measured the atmospheric parameters of GD 246 by fitting the Balmer lines with the use of either LTE or non-LTE (NLTE) stellar atmosphere models. They obtained effective temperatures and gravities in the ranges $53,000 \text{ K} \leq T_{\text{eff}} \leq 60,000 \text{ K}$ and $7.7 \leq \log g \leq 8.0$ (see, e.g., Finley, Koester, & Basri 1997; Marsh et al. 1997; Vennes et al. 1997; Barstow, Hubeny, & Holberg 1998; Napiwotzki et al. 1999). For our analysis of the stellar continuum in the vicinity of the H I $\text{Ly}\alpha$ profile, and knowing that NLTE effects are important in the core of $\text{Ly}\alpha$, we adopted the atmospheric parameters determined by Napiwotzki et al. (1999), who based their results on pure hydrogen NLTE models. They obtained $T_{\text{eff}} = 53,088 \pm 968 \text{ K}$ and $\log g = 7.85 \pm 0.07$ (1σ error bars). Napiwotzki et al. (1999) pointed out that systematic uncertainties, which may result from the extraction of the spectrum, the flux calibration, or the normalization, are much larger than the statistical errors. To take into account these systematic errors, we considered the 1σ errors on T_{eff} and $\log g$ to be 3000 K and 0.15 , respectively. The grid of models that we computed to estimate the stellar $\text{Ly}\alpha$ line includes these errors ($T_{\text{eff}} = 50,000, 53,000, \text{ and } 56,000 \text{ K}$; $\log g = 7.70, 7.85, \text{ and } 8.0$).

Observations in the EUV, FUV, and UV wavelength bands reveal that the atmosphere of GD 246 contains low abundances of elements heavier than hydrogen. For instance, Chayer et al. (2001) and Wolff et al. (2001) analyzed the *International Ultraviolet Explorer* (*IUE*) and *FUSE* spectra of GD 246 and measured very low abundances of carbon, silicon, and phosphorus. Wolff et al. (1998) analyzed the *Extreme Ultraviolet Explorer* (*EUVE*) spectrum of GD 246 with LTE metal line-blanketed models and concluded that the star had a lower metallicity than G191-B2B, which is the metal-rich white dwarf prototype. Dupuis, Vennes, & Chayer (2000) reported the detection of Fe VI absorption features in the *Chandra* LETG spectrum of GD 246. But the nondetection of Fe V in the STIS spectrum of GD 246 puts an upper limit on the iron abundance of $\log(\text{Fe}/\text{H}) \leq -6.0$. We expect that these small traces of heavy elements do not modify the physical structure of the atmosphere of the star and consequently do not influence the $\text{Ly}\alpha$ line profile. Therefore, we computed pure hydrogen NLTE stellar atmospheres models to describe the stellar $\text{Ly}\alpha$ line.

Determining the H I column density with different stellar models places more credible error bars on $N(\text{H I})$ than using a single stellar model. The statistical uncertainties are derived by using the best stellar model, and the systematic uncertainties associated to the stellar models are estimated by considering the most extreme stellar parameters, i.e., those parameters that yield the strongest and weakest stellar $\text{Ly}\alpha$. Figure 7 illustrates such stellar $\text{Ly}\alpha$ profiles. The figure shows that the best stellar model (model *a*: $T_{\text{eff}} = 53,000 \text{ K}$ and $\log g = 7.85$) produces a $\text{Ly}\alpha$ line profile that is between the strongest $\text{Ly}\alpha$ line (model *b*: $T_{\text{eff}} = 50,000 \text{ K}$ and $\log g = 7.70$) and the weakest one (model *c*: $T_{\text{eff}} = 56,000 \text{ K}$ and $\log g = 8.00$).

4.2.2. $\text{Ly}\alpha$ Profile Fitting

Wolff et al. (2001) determined that the photospheric lines of this star are separated by $v = -6 \text{ km s}^{-1}$ from the interstellar lines. To take into account the relative shift between interstellar and stellar lines, we align the model and the data in three different ways: displacing the model by $-10, 0, \text{ and } +10 \text{ km s}^{-1}$ relative to the data. By comparing the stellar $\text{Ly}\alpha$ model with the data, we took into consideration the radial velocity of GD 246, which includes its velocity with respect to the Sun and its gravitational redshift. Because of the large breadth of the interstellar H I absorption, displacing the model and the data by 10 km s^{-1} does not lead to any difference in the measured H I column density from our fits. For each stellar model computed, the E140M spectrum of H I $\text{Ly}\alpha$ is normalized by the stellar model prior to profile fitting (see Fig. 7, bottom panel). In addition, a second-order polynomial is used to model the continuum after normalization by the model atmosphere, to take into account uncertainties in the instrument sensitivity. Using the best-fit stellar model, we perform two fits (see § 3 for a description of the fitting process) of the H I $\text{Ly}\alpha$ profile using both a 2 pixel single-Gaussian LSF and the tabulated STIS LSF for the $0''.02 \times 0''.09$ slit. There are no differences in the results using the two LSFs. We derive $\log N(\text{H I}) = 19.11 \pm 0.02 \pm 0.03$ (2σ), where the first error bars reflect the uncertainties associated with the different stellar models and the second error bars take into account the statistical uncertainties when using the best-fit model. We find, then,

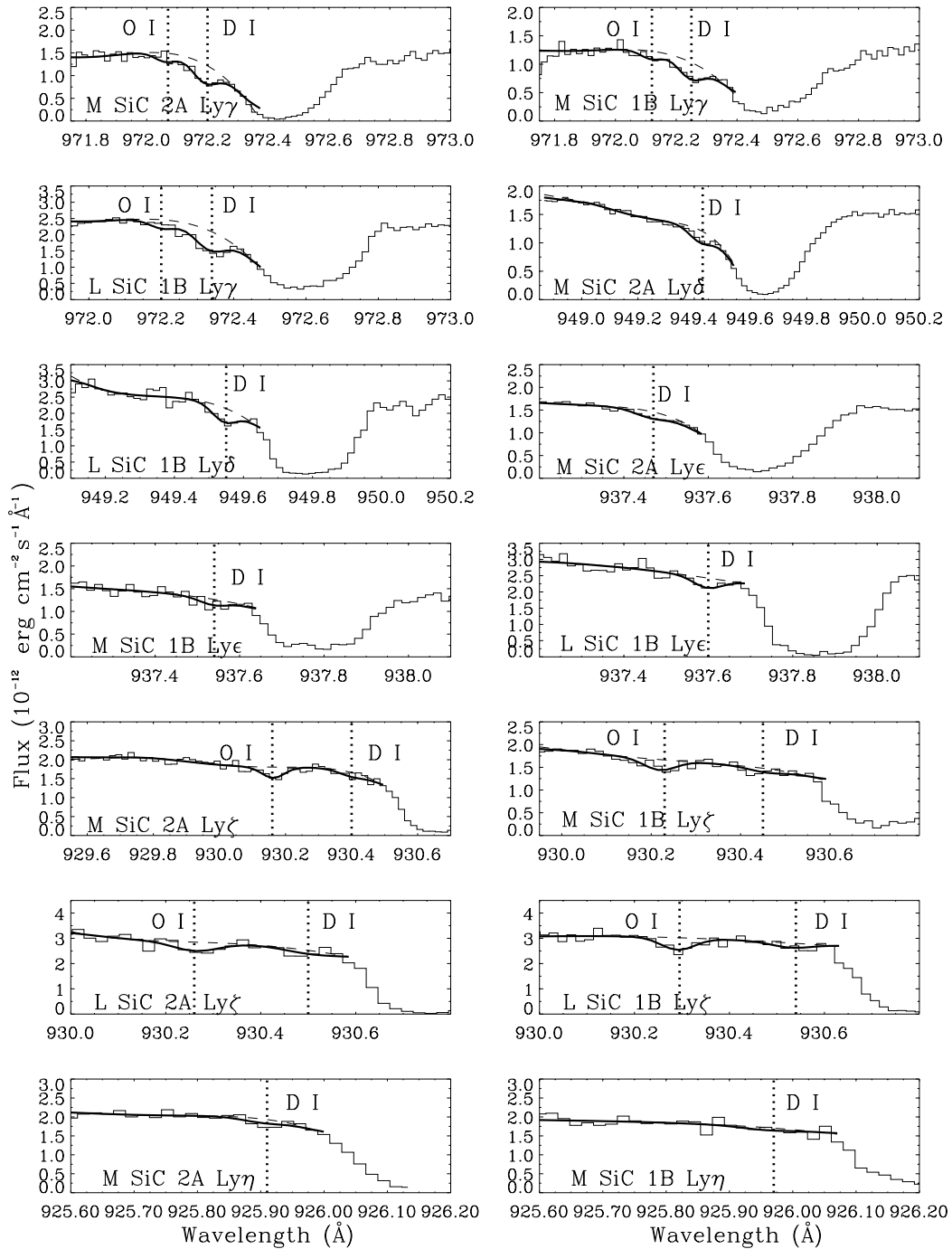


FIG. 6.—Fits to the D I lines used in the analysis for GD 246. “L” and “M” stand for LWRS and MDRS data, respectively. D I Ly β was not used in the analysis because of contamination by geocoronal emission. Vertical lines mark the centroids of the fitted D I and O I absorption lines.

$\log N(\text{H I}) = 19.11 \pm 0.05$ (2σ), by taking a conservative approach to combine the two different uncertainties. Our H I column density is in close agreement with the value of $\log N(\text{H I}) = 19.12^{+0.02}_{-0.10}$ (1σ) derived from *EUVE* data by Barstow et al. (1997) using stellar models incorporating heavy elements.

Lemoine et al. (2002) have expressed concern over the presence of weak H I components, which could perturb or bias the measurement of $N(\text{H I})$ but would not be detected in other species because of their weak column density. Vidal-Madjar & Ferlet (2002) reanalyzed the Capella line of

sight and showed a significant increase in the uncertainty due to this effect. However, they also concluded that for warm gas with column densities of H I above 10^{19} cm^{-2} , the H I column density evaluation is more credible than for absorbers with lower column densities. We have tried to investigate the possible effect of additional weak, hot components on the determination of $N(\text{H I})$. In order to do so, we added one or two additional components in H I only and performed the fits to Ly α and Ly β . For Ly β we used the blue wing of night-only data, since the geocoronal emission in this region distorts the shape of the red wing of the profile.

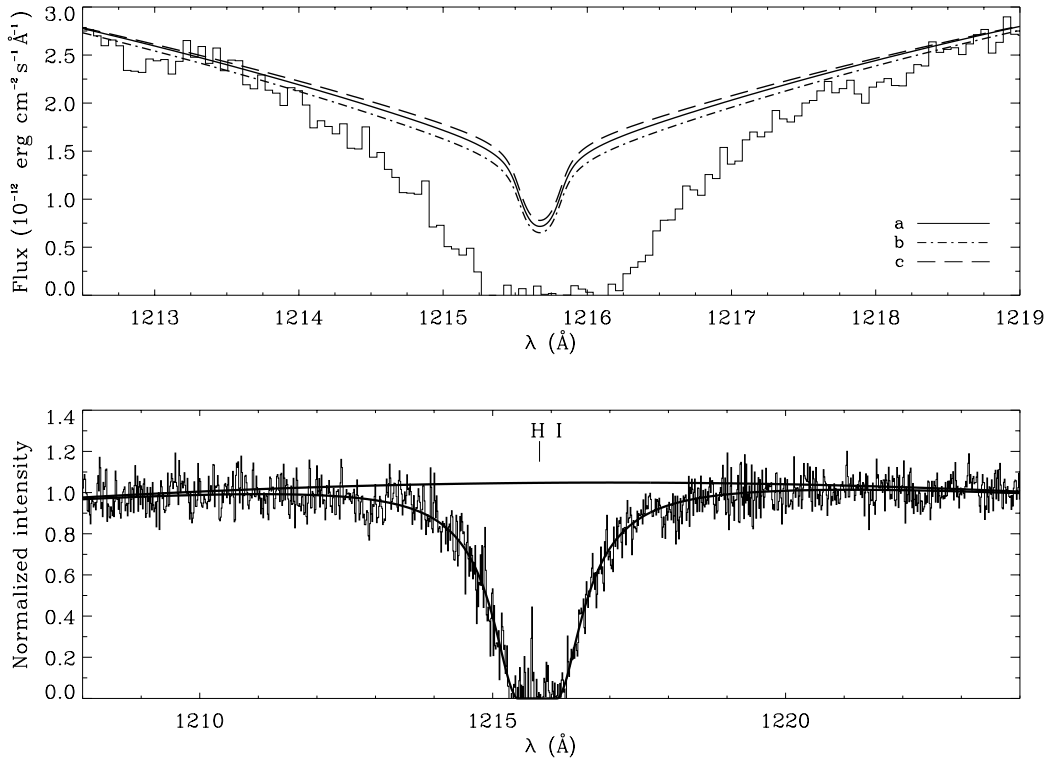


FIG. 7.—*Top*: Interstellar H I Ly α toward GD 246 (data binned by 4 for display purposes only). The histogram shows the co-added STIS E140M observations of GD 246. Model *a* is the best-fit stellar model, with $T_{\text{eff}} = 53,000$ K and $\log g = 7.85$ (see text for discussion). Model *b* was computed with $T_{\text{eff}} = 50,000$ K and $\log g = 7.7$ and model *c* with $T_{\text{eff}} = 56,000$ K and $\log g = 8.0$. *Bottom*: Fit to the H I Ly α profile after division by the best-fit stellar model (model *a*; see text) and with the continuum modeled by a second-order polynomial.

We were not able to find weak, hot components of the type described by Lemoine et al. (2002), for which both Ly α and Ly β profiles agreed. As pointed out by Lemoine et al. (2002), these weak, hot components are very difficult to find, and it is possible that we might have missed them, thus underestimating the uncertainties quoted for $N(\text{H I})$. However, we think that this is unlikely, given the conclusions of Vidal-Madjar & Ferlet (2002).

5. ANALYSIS OF THE WD 2331–475, HZ 21, AND LAN 23 LINES OF SIGHT

WD 2331–475 is a hot DA white dwarf with $T_{\text{eff}} = 51,800$ K and $\log g = 7.79$ (Vennes et al. 1997). A few stellar lines of Si IV, P IV–V, and S IV–V are present in the data. There are no *HST* observations of this star, and the quality of the *IUE* data is not high enough for a reliable H I measurement.

HZ 21 is a helium-rich (DO) white dwarf showing only a few stellar lines of N IV, P V, Si IV, and S VI in the *FUSE* data. Figure 3 shows the broad stellar He II absorption lines due to transitions from the energy level $n = 2$. With effective temperature $T_{\text{eff}} = 53,000$ K and gravity $\log g = 7.8$ (Dreizler & Werner 1996), this low-metallicity star provides a smooth stellar continuum against which the interstellar lines are clearly seen. No molecular hydrogen is detected along this line of sight. There is probably more than one velocity component along this line of sight, considering the large distance to this star, $d = 115$ pc. Unfortunately, no *HST* observations of this star with sufficient resolution to

resolve the velocity structure exist. In addition, this star has not been observed by *EUVE*, and the quality of the *IUE* data is not high enough for a reliable H I measurement.

Lan 23 is a DA white dwarf with an effective temperature of $T_{\text{eff}} = 59,360$ K and $\log g = 7.84$ (Vennes et al. 1997). Stellar lines from the ground states of O VI and S VI and from an excited state of C III are seen in the *FUSE* spectra of this star. This star has not been observed by *HST*, so we do not have information about the velocity structure along this line of sight. Considering that this star is at a distance of $d = 122$ pc, several absorption components would be expected. Wolff et al. (1999) have used *EUVE* data to measure the interstellar H I column density along this line of sight. Because of the high interstellar column density of H I and also some unknown opacity in the white dwarf itself, the *EUVE* flux is very small, which implies a large uncertainty in the determination of the interstellar H I column density. They find $\log N(\text{H I}) = 19.89^{+0.31}_{-0.04}$, where the error bars quoted include uncertainties in the photospheric composition. These authors do not mention the confidence level corresponding to the quoted error bars, so we assume these are approximately 1σ uncertainties, which we use to calculate the 2σ uncertainties quoted in Table 6.

5.1. Column Density Determinations

5.1.1. WD 2331–475

For this line of sight we measure the column densities of D I, C II*, N I, O I, Si II, P II, Ar I, and Fe II, using PF, COG, and AOD. Both PF1 and PF2, discussed above, were used. We first attempted to fit the data with a single absorption

TABLE 6
RATIOS OF COLUMN DENSITIES

Star	D I/H I ($\times 10^{-5}$)	O I/H I ($\times 10^{-4}$)	D I/O I ($\times 10^{-2}$)	N I/H I ($\times 10^{-5}$)	D I/N I ($\times 10^{-1}$)	O I/N I
GD 246	$1.51^{+0.39}_{-0.33}$	$3.63^{+0.77}_{-0.67}$	$4.17^{+1.21}_{-1.00}$	$4.37^{+0.84}_{-0.74}$	$3.47^{+0.95}_{-0.79}$	$8.32^{+1.91}_{-1.64}$
WD 2331–475	$5.13^{+2.20}_{-1.69}$...	$4.57^{+1.88}_{-1.45}$	$8.91^{+3.45}_{-2.71}$
HZ 21	$4.57^{+2.22}_{-1.63}$...	$4.27^{+1.96}_{-1.44}$	$9.33^{+3.07}_{-2.48}$
Lan 23	$2.19^{+4.64}_{-0.68}$	$6.76^{+15.5}_{-4.10}$	$3.24^{+3.27}_{-2.06}$	$6.92^{+14.7}_{-2.33}$	$3.16^{+1.56}_{-1.23}$	$9.77^{+9.89}_{-6.37}$

NOTE.—All uncertainties are 2σ .

component. This resulted in a large underestimation of the D I, N I, and O I column densities when compared with the COG and AOD results. A closer inspection of the data revealed that some of the stronger lines have a wing extending toward negative velocities. Profile fitting with two components resulted in column density values within 1σ of the COG and AOD results. We determined that the data are better represented by two absorption components separated by $\sim 14 \text{ km s}^{-1}$, with similar Doppler parameters b . Figure 8 displays the two-component fit to C II*, N I, and Fe II. This component structure is also used for D I, O I, Si II, P II, and Ar I, not shown in Figure 8. The fit to D I (using PF2) is

shown in Figure 9. The column densities adopted are given in Table 5.

5.1.2. HZ 21 and Lan 23

For both of these sight lines our PF analyses assume the presence of only one interstellar component. We fit the species D I, N I, O I, Si II, P II, Ar I, and Fe II in HZ 21 and D I, N I, O I, and Fe II in Lan 23. For the Lan 23 line of sight we include an extra component containing H₂, described in more detail in § 5.2.

In the case of HZ 21, the uncertainties introduced by the presence of broad stellar He II absorption in the neighborhood of the D I lines should be negligible compared to our final error bars on the column density of D I. Dreizler & Werner (1996) determined an upper limit on the hydrogen-to-helium abundance ratio of $\text{H}/\text{He} < 0.1$ in the atmosphere of the helium-rich white dwarf HZ 21. To take into consideration the effects of the stellar helium abundance on the column density of D I, we computed two stellar models with hydrogen-to-helium abundance ratios of $\text{H}/\text{He} = 0.1$ and 0.01 . Figure 10 displays two stellar models computed with $T_{\text{eff}} = 53,000 \text{ K}$ and $\log g = 7.8$, but different hydrogen-to-helium abundance ratios. Model *a* has $\text{H}/\text{He} = 0.1$, and model *b* has $\text{H}/\text{He} = 0.01$. In both models the He II stellar absorption is so broad that it does not affect the underlying D I absorption.

There are many oxygen transitions in the *FUSE* bandpass, covering a wide range of oscillator strengths. Unfortunately, at the high column density of O I in Lan 23 and with the low signal-to-noise ratio of the data, it is difficult to find nonsaturated O I lines that are suitable for our analysis. We find only two such lines, $\lambda 919.917$ and $\lambda 974.070$, which span more than 1 dex in $\log f\lambda$. This is the source of the large error bars for the O I column density along this line of sight.

Fits for D I (using PF2) are presented in Figures 11 (HZ 21) and 12 (Lan 23). The column densities, found by combining the results of the two different analyses (PF1 and PF2), are given in Table 5.

5.2. Interstellar H₂ toward Lan 23

Absorption arising from H₂ rotational levels $J = 0-3$ is clearly seen in the *FUSE* spectra of Lan 23. Some H₂ lines are blended with D I and can be a problem for the measurement of the D I column density. We determine the column density of each J -level by fitting a single-component COG to lines from $J = 0$ to 3 simultaneously, assuming the same b -value for all J -levels. From the COG we obtain a Doppler parameter, $b = 4.1^{+0.8}_{-0.6} \text{ km s}^{-1}$ (2σ). The b -value obtained

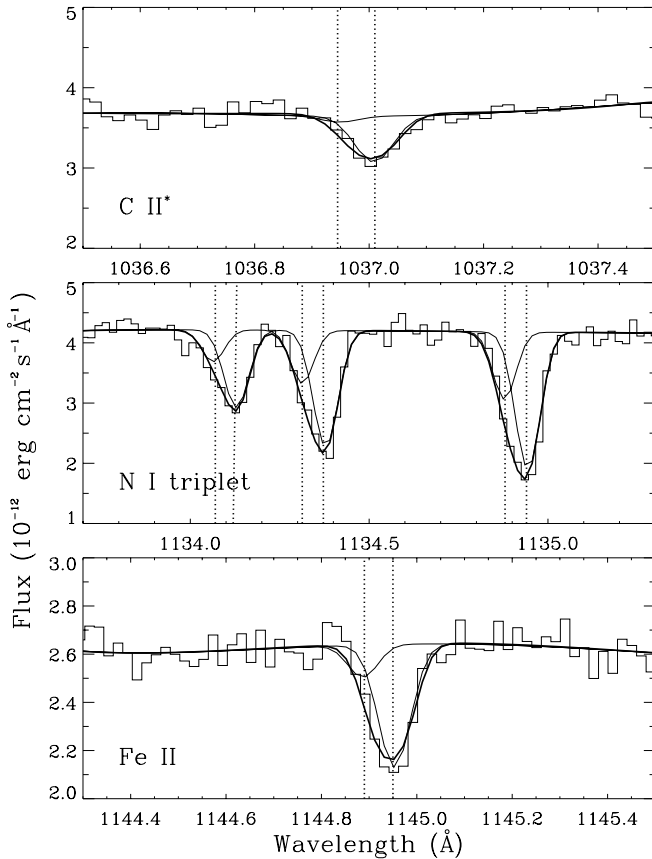


FIG. 8.—Double-component fits to some metal lines used in the analysis for WD 2331–475. In this case, the use of a single component showed significant differences between the results from the PF and COG analyses. In some cases, the discrepancy between the single-component fit and the data was apparent upon inspection of the blue side of the absorption line. Vertical lines mark the centroids of the two components for C II*, N I, and Fe II.

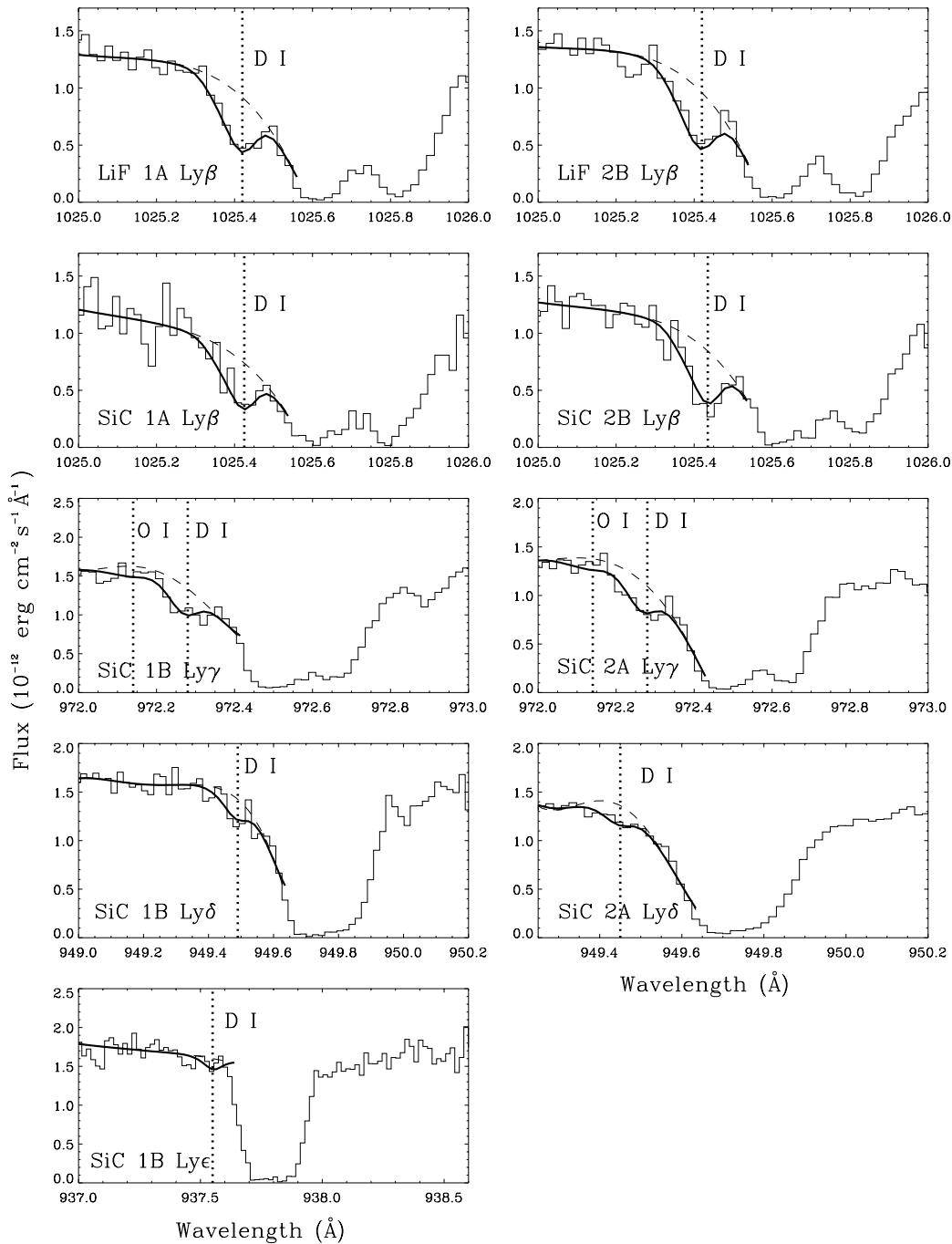


FIG. 9.—Fits to the D I lines used in the analysis for WD 2331–475, all from the P1044203 observation. For D I, Ly β -only night data were used, in order to reduce the geocoronal emission. Some emission is still present between 972.5 and 972.7 Å and 1025.6 and 1025.8 Å. Vertical lines mark the centroids of the fitted D I and O I absorption lines.

from the COG is then used as a constraint in the PF analysis of H₂, described in the paragraph below.

We also determine the H₂ column density by including unsaturated H₂ $J = 0-3$ lines in our PF analysis of this line of sight. The column density for each rotational level is determined independently, with no assumption about the rotational temperature of the gas. To allow for the possibility that this small amount of molecular hydrogen does not reside in the same gas as the D I, the velocity centroid of the H₂ is free to assume a different value from that of the D I.

Column densities obtained with PF and COG are displayed in Table 7. The total H₂ column density along this

line of sight is of the order $\log N(\text{H}_2) \sim 15$. The derived excitation temperatures are $T_{01} \approx 291$ K, $T_{12} \approx 324$ K, and $T_{23} \approx 240$ K; however, formal relative contributions of UV pumping versus collisional excitation have not been explored.

6. SYSTEMATIC EFFECTS

There are several systematic effects in the *FUSE* data that can contribute to uncertainties in the estimated column densities and are not directly included in our determination of the error bars. Below we discuss the most important

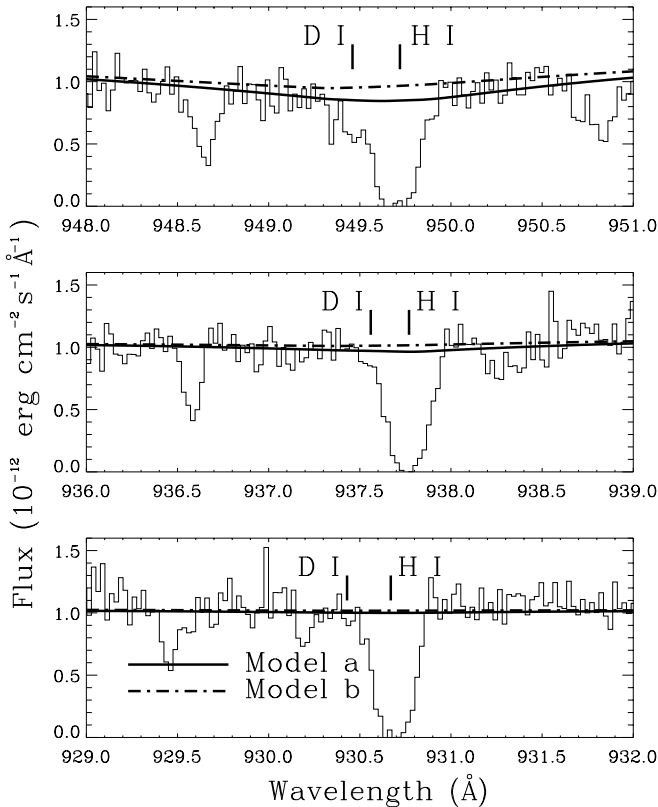


FIG. 10.—Comparison between two models and the *FUSE* data of the helium-rich white dwarf HZ 21 in the regions of the D I $\lambda\lambda$ 930, 937, and 949 lines. The models are computed with $T_{\text{eff}} = 53,000$ K, $\log g = 7.8$, and two stellar hydrogen abundances $N(\text{H})/N(\text{He}) = 0.1$ (model *a*) and $N(\text{H})/N(\text{He}) = 0.01$ (model *b*). Vertical lines mark the positions of D I and H I.

systematic effects in detail, how they can affect our data, and how we address these problems in our PF analysis. For additional discussion of systematic effects in D/H measurements such as these, we refer the reader to Hébrard et al. (2002), Kruk et al. (2002), and Moos et al. (2002).

6.1. Fixed-Pattern Noise

Fixed-pattern noise associated with the detectors can distort profile shapes and alter the equivalent widths of the absorption lines. The four-channel design of *FUSE* provides at least two (sometimes four) independent spectra of most of the lines used in the analysis. By comparing data from multiple segments, multiple observations, and multiple slits, we are able to identify the absorption profiles that suffer from large (compared to the statistical noise) fixed-pattern noise artifacts and exclude them from our fits. However, small effects cannot be ruled out.

6.2. Background and Line-Spread Function

Although a comprehensive study of the LSF for the *FUSE* instrument is not yet available, preliminary studies indicate that it is composed of two (Gaussian) components. The narrow component has an FWHM of ~ 15 – 20 km s^{-1} , and the broad component contains 20%–30% of the total LSF area (with a large portion of this broad component falling under the narrow core of the LSF). This broad component is responsible for the residual light in the cores of

saturated lines (e.g., the high-order Lyman lines in Figs. 1–4); in addition, there may be scattered light. We use a single-Gaussian LSF in our analysis and adopt a small zero flux level shift to account for the residual light in lines close to the Ly α series of H I, for which this effect is more visible. Because we are fitting only nonsaturated lines, any residual errors in this correction for the tail of the LSF should not affect our derived column densities in a significant way. To the extent that this small amount of residual light is due to the LSF, it may produce small systematic changes in the derived column densities, but such effects are expected to be small compared to the derived uncertainties.

6.3. Oscillator Strength Uncertainties

While oscillator strengths (f -values) of the D I lines are well known, the same may not be true for other elements, such as N I and O I. By fitting multiple lines of the same species at the same time, we are able to remove the lines that stand out as a poor fit and average out the small errors of the other lines in the final result. A case in which the uncertainty in an O I f -value might pose a problem is in the determination of the O I column density for the Lan 23 line of sight. For this star, only two nonsaturated lines have enough signal-to-noise ratio to be useful in our analysis: $\lambda 974.07$ (very weak, $f = 1.56 \times 10^{-5}$ and partially blended with H₂ [$J = 2$]) and $\lambda 919.9$ ($f = 1.76 \times 10^{-4}$).

In other analyses of O I for which $\lambda 919.9$ was used (e.g., Hébrard et al. 2002), this line did not stand out as having a large problem with its f -value. A test in which the O I column density was determined by fitting each line individually showed a 20% dispersion around the value obtained with a fit to all the lines simultaneously (see Hébrard et al. 2002). Since the error bars derived for $N(\text{O I})$ toward Lan 23 are large, it is unlikely that the uncertainty in the f -values of the O I lines used here plays a large role in our measurement of $N(\text{O I})$.

We measure the column density of Ar I in the four lines of sight using only one transition of Ar I ($\lambda 1048.2198$), because the other one ($\lambda 1066.6599$) is blended with photospheric Si IV. Any uncertainties in the f -value of this transition will affect our column density of Ar I.

6.4. Number of Interstellar Components along the Line of Sight

In § 4.2.2, we discussed the potential effects of weak, hot H I components on the determination of $N(\text{H I})$ for GD 246. Because the H I column density is greater than 10^{19} cm $^{-2}$, such effects are probably small. For all species a major difficulty associated with measuring column densities is the presence of unresolved, overlapping absorption components along the line of sight. Small-scale velocity structure has been seen in, among others, K I and Na I ultra-high-resolution surveys, for relatively small path lengths (see, e.g., Welty & Hobbs 2001). The problem arises if the physical conditions in the different absorption components are significantly different. In a mix of cold (narrow) and warm (broad) components, each with approximately the same column density, the cold component will become saturated before the warm component. Because the components are unresolved, the absorption profile resulting from the sum of the two components may appear to be unsaturated, thus leading to an incorrect estimate of the total column density. For GD 246 the STIS data show no evidence of such

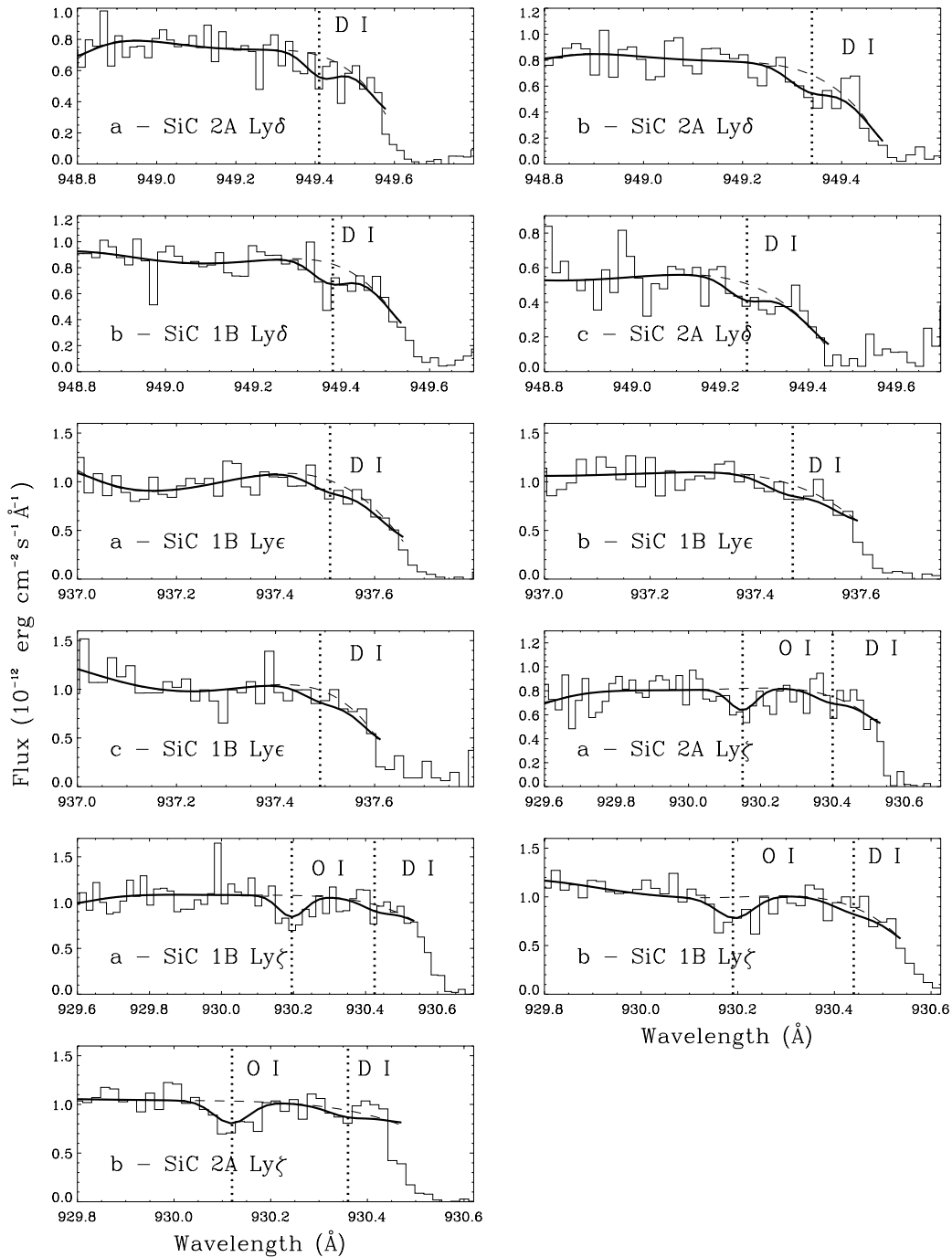


FIG. 11.—Fits to the D I lines used in the analysis for HZ 21. Labels “a,” “b,” and “c” represent data from P204 MDRS, P204 LWRS, and M108 LWRS, respectively. Vertical lines mark the centroids of the fitted D I and O I absorption lines.

material. Lan 23 has a low H_2 column density ($\sim 10^{15} \text{ cm}^{-2}$), and the other white dwarfs show no evidence of H_2 in their *FUSE* spectra. However, without ultra-high-resolution data, this systematic effect can never be completely ruled out.

6.5. Profile Contamination by Unknown Stellar Features

Although improbable, some of the lines used in our analysis could be contaminated by unknown stellar features (see, e.g., Sonneborn et al. 2002; Friedman et al. 2002). Since the four white dwarfs studied here are all metal-poor, we do

not believe that this is a significant concern. Photospheric Si IV is present in the spectra of the white dwarfs studied here and is blended with Ar I $\lambda 1066.66$; this Ar I transition is not used in our analysis.

6.6. Effect on Column Density Ratios

We believe that the systematic effects discussed above are generally small. It is possible that these effects could be of importance for the column densities with small statistical uncertainties. However, it is unlikely that they will be of significance for the column density ratios discussed in § 7.

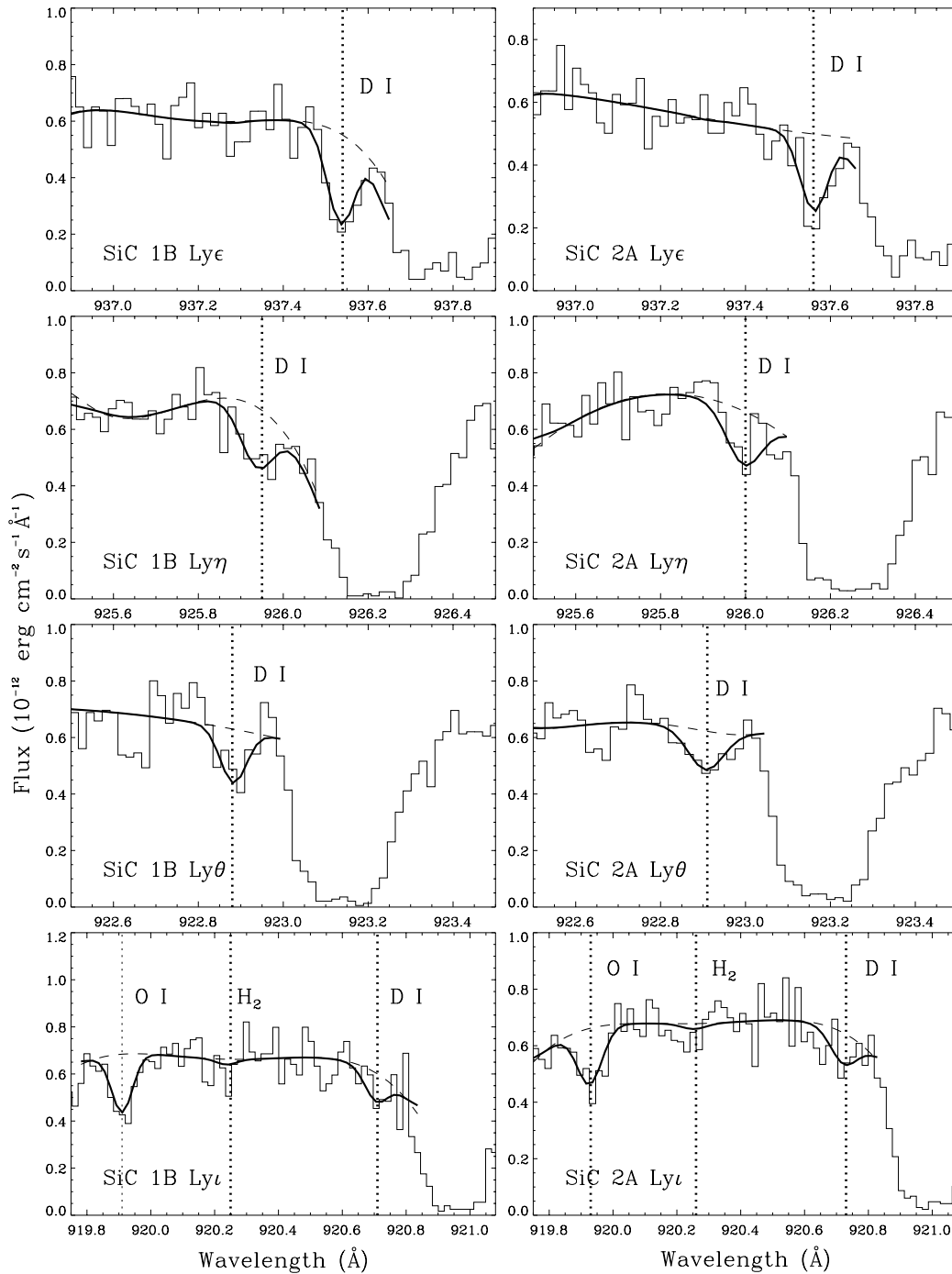


FIG. 12.—Same as Fig. 11, but for Lan 23. Vertical lines mark the centroids of the fitted D I, O I, and H₂ absorption lines.

7. RESULTS AND DISCUSSION

In § 7.1, we discuss the line of sight to the four stars in the context of the Local Bubble. In § 7.2, we compare the total column density ratios of D/H, O/H, and N/H for GD 246, WD 2331–475, HZ 21, and Lan 23 to values found for other lines of sight in the local ISM and discuss the implications of using O and N as tracers of H for these lines of sight. In § 7.3, we combine the ratios derived here with previously published *FUSE* ratios, deriving revised *FUSE* mean ratios. In § 7.4, we discuss the mean D/O ratio inside the Local Bubble. Section 7.5 presents a more detailed discussion of the GD 246 line of sight. Because we have information on

the velocity structure along this line of sight, we can separate the LIC and Local Bubble contributions to the total column densities and draw more detailed conclusions about the distribution of material along the line of sight.

7.1. Local Bubble

Sfeir et al. (1999) have used absorption-line studies of Na I to approximately map the contours of the Local Bubble. They found a cavity, with a radius between 65 and 250 pc (depending on the direction), that is delineated by a sharp gradient in the neutral gas column density with increasing radius, a dense neutral gas “wall.” Sfeir et al.

TABLE 7
H₂ COLUMN DENSITIES IN LAN 23

Rotational Level	Profile Fitting ^a [log $N(\text{H}_2)$]	Curve of Growth ^b [log $N(\text{H}_2)$]
$J = 0$	$14.35^{+0.05}_{-0.09}$	$14.12^{+0.08}_{-0.09}$
$J = 1$	$14.97^{+0.07}_{-0.09}$	14.89 ± 0.11
$J = 2$	$14.32^{+0.09}_{-0.13}$	$14.20^{+0.08}_{-0.05}$
$J = 3$	13.95 ± 0.07	$13.93^{+0.11}_{-0.10}$

NOTE.—All uncertainties are 2σ .

^a The b -value of the fit was constrained to 4.1 km s^{-1} . The errors quoted do not include a contribution from errors in the b -value.

^b All lines are fitted simultaneously, yielding $b = 4.1^{+0.8}_{-0.6} \text{ km s}^{-1}$ (2σ).

(1999) quote an equivalent width of $20 \text{ m}\text{\AA}$ of Na I $\lambda 5891.59$ as corresponding to $\log N(\text{H I}) \sim 19.3$, which is used as a rough estimate of a plausible Local Bubble boundary. According to their map of the Local Bubble, the GD 246 line of sight does not penetrate the wall, as it lies between the 5 and $20 \text{ m}\text{\AA}$ Na I $\lambda 5889.95$ contours. Although the uncertainty in the distance to GD 246 (and for the other three white dwarfs, for that matter) makes this result ambiguous, $\log N(\text{H I}) = 19.11 \pm 0.05$, implying that GD 246 is likely close to the wall of the Local Bubble but does not penetrate the higher density regions beyond. The lines of sight to WD 2331–475 and HZ 21 do not penetrate the wall, either; WD 2331–475 lies inside the $20 \text{ m}\text{\AA}$ contour, and HZ 21 lies between the 5 and $10 \text{ m}\text{\AA}$ contours. In addition, as shown in the next section, the measured O I column density toward both WD 2331–475 and HZ 21 implies an H I column density similar to that toward GD 246. The Lan 23 line of sight is located between the 20 and $50 \text{ m}\text{\AA}$ Na I $\lambda 5889.95$ contours and has a high H I column density; it likely penetrates the wall of the Local Bubble.

7.2. O/H, D/H, and N/H Ratios

Table 6 summarizes the column density ratios for several species along the four lines of sight studied in this work. For GD 246 we find $\text{O I}/\text{H I} = 3.63^{+0.77}_{-0.67} \times 10^{-4}$. This ratio is in agreement with the O I/H I ratio derived by Meyer, Jura, & Cardelli (1998) of $\text{O I}/\text{H I} = (3.43 \pm 0.30) \times 10^{-4}$ (using the f -value updated to $f = 1.16 \times 10^{-6}$ from Welty et al. 1999).

Reliable H I measurements are not available for WD 2331–475, HZ 21, or Lan 23. However, the constancy of the O/H ratio discussed above enables us to derive an approximate column density for H I using O I. Using the Meyer et al. (1998) interstellar O I abundance and the O I column density along each line of sight, we estimate $\log N(\text{H I}) = 18.94$ for WD 2331–475, 19.20 for HZ 21, and 20.16 for Lan 23.

Using the $N(\text{H I})$ obtained this way and our measured $N(\text{D I})$, we obtain $\text{D I}/\text{H I} \sim 1.8 \times 10^{-5}$, 1.6×10^{-5} , and 1.2×10^{-5} for WD 2331–475, HZ 21, and Lan 23, respectively. The uncertainties in the O I columns used to derive the H I column densities are large enough that the differences between the derived D/H ratios for these stars and the Moos et al. (2002) weighted mean of $\text{D}/\text{H} = (1.52 \pm 0.15) \times 10^{-5}$ are not significant. The D/H ratio for GD 246 is discussed in § 7.5.

Using the Meyer, Cardelli, & Sofia (1997) interstellar abundance of nitrogen, $\text{N}/\text{H} = (7.5 \pm 0.8) \times 10^{-5}$, and our

measured N I column density leads to estimated values of $\log N(\text{H I}) = 18.87$ for GD 246, 18.65 for WD 2331–475, 18.89 for HZ 21, and 19.82 for Lan 23. The H I column density derived using the N I column density is in all four cases only $\sim 50\%$ of the H I column density determined using the O I abundance, implying that the N I column densities are low. It is possible that the N along these lines of sight is $\sim 50\%$ ionized. This effect has been seen for other sight lines as well (see Jenkins et al. 2000; Lehner et al. 2002; Moos et al. 2002). For GD 246 we measure $\text{N I}/\text{H I} = 4.37^{+0.84}_{-0.74} \times 10^{-5}$, which is a factor of 1.7 times smaller than the Meyer et al. (1997) value but is in close agreement with the weighted mean of the *FUSE* sight lines, $\text{N I}/\text{H I} = (4.24 \pm 0.62) \times 10^{-5}$ (see Moos et al. 2002).

The ionization fraction of N I along a line of sight can be estimated directly by measuring the N II and N III column densities, as both N II and N III have transitions in the *FUSE* bandpass. However, for our sight lines the N II transitions available in the *FUSE* bandpass are saturated, and N III cannot be determined, since it is blended with interstellar Si II and sometimes with photospheric N III. Hébrard et al. (2002), Kruk et al. (2002), and Wood et al. (2002) have been able to measure the column density of N II (and sometimes N III) along three different lines of sight and found that in all cases it was larger than the column density of N I, providing a better agreement between $(\text{N}/\text{H})_{\text{total}}$ within 100 pc and $\text{N I}/\text{H}_{\text{total}}$ for larger path lengths.

7.3. Revised *FUSE* Ratios

In Table 8, we combine the ratios derived here with the Moos et al. (2002) ratios for $\text{D I}/\text{H I}$, $\text{O I}/\text{H I}$, $\text{N I}/\text{H I}$, $\text{D I}/\text{N I}$, $\text{D I}/\text{O I}$, and $\text{O I}/\text{N I}$ and present the Meyer et al. (1997, 1998) N/H and O/H values for comparison. We present also the χ^2_ν test for a single mean value. The values quoted in Table 8 are the weighted means and uncertainty in the means, where we use the largest of the lower and upper error bars of each individual ratio to compute the weighted mean. We use 1σ error bars in this subsection, in order to make it easier to compare the different lines of sight among themselves. For Lan 23 values only the $\text{D I}/\text{N I}$ value is used, because of the large error bars for the other ratios associated with this line of sight. As a result of combining our ratios with the Moos et al. (2002) values, the weighted means increase by 0% – 5% .

The mean $\text{D I}/\text{O I}$ ratio is $(4.06 \pm 0.17) \times 10^{-2}$, with $\chi^2_\nu = 1.9$ ($\nu = 9$). The mean $\text{D I}/\text{N I}$ ratio now computed with 10 lines of sight is $(3.41 \pm 0.15) \times 10^{-1}$, with $\chi^2_\nu = 2.2$ ($\nu = 9$).

7.4. D/O Ratio inside the Local Bubble

Hébrard et al. (2001) and Moos et al. (2002) have found a nearly constant D/O ratio inside the Local Bubble, indicating that D/O traces the D/H ratio. The weighted mean of the five *FUSE* sight lines within the Local Bubble (Moos et al. 2002) is $(3.76 \pm 0.20) \times 10^{-2}$ (1σ in the mean). When we combine the D/O ratios derived here (the Lan 23 value is not included, as it is likely outside the Local Bubble) with the Local Bubble *FUSE* results from Moos et al. (2002), we derive a weighted mean and uncertainty in the mean of $\text{D I}/\text{O I} = (3.87 \pm 0.18) \times 10^{-2}$ (1σ in the mean), with $\chi^2_\nu = 0.96$ ($\nu = 7$), reinforcing the Moos et al. (2002) conclusion that the variability of the data is consistent with the uncertainties; i.e., the $\text{D I}/\text{O I}$ ratio is constant within the

TABLE 8
REVISED *FUSE* RATIOS AND COMPARISON WITH OTHER MEASUREMENTS

Ratio	Moos et al. 2002 + This Work ^a	χ^2_ν for Mean	ν^b (dof)	Meyer et al. 1997, 1998 ^c
D I/H I.....	$(1.52 \pm 0.07) \times 10^{-5}$ (0%)	1.0	5 (4)	...
O I/H I.....	$(3.17 \pm 0.19) \times 10^{-4}$ (+5%)	3.5	5 (4)	$(3.43 \pm 0.15) \times 10^{-4}$
D I/O I.....	$(4.06 \pm 0.17) \times 10^{-2}$ (+2%)	1.9	9 (6)	...
N I/H I.....	$(4.28 \pm 0.25) \times 10^{-5}$ (+1%)	1.4	4 (3)	$(7.5 \pm 0.4) \times 10^{-5}$
D I/N I.....	$(3.41 \pm 0.15) \times 10^{-1}$ (+1%)	2.2	9 (5)	...
O I/N I.....	8.23 ± 0.38 (+2%)	2.9	8 (5)	4.6 ± 0.3

NOTE.—All uncertainties in this table are 1σ in the mean.

^a Mean values and uncertainties in the mean. The values in parentheses correspond to the percent increase from the Moos et al. 2002 values. Our values are combined with those from Moos et al. 2002 by taking a weighted mean. We use the largest of the lower and upper error bars of each individual ratio to compute the weighted mean.

^b ν = number of sight lines $- 1$. Values in parentheses represent the number of degrees of freedom in Moos et al. 2002.

^c The values correspond to O/H and N/H; the uncertainties quoted are errors in the mean. O/N calculated here from O/H and N/H.

Local Bubble. The D I/O I ratio inside the Local Bubble will be discussed in more detail by G. Hébrard et al. (2003, in preparation).

7.5. GD 246

Absorption by at least two different components, separated by ~ 9 km s⁻¹, is clearly seen along the GD 246 sight line in the high-resolution STIS echelle data of N I, S II, and Si II (see Fig. 5). The stronger component (component 1), seen at -9.76 km s⁻¹, contains 86%, 82%, and 79% of the total column densities of N I, S II, and Si II, respectively, along this line of sight. The velocity of component 2, $v_2 = -0.63$ km s⁻¹, is consistent with the expected velocity of the LIC along this line of sight ($+2.46 \pm 1.84$ km s⁻¹; Lallement et al. 1995) when the zero-point velocity uncertainty in STIS E140H data is taken into account ($\Delta v \sim 0.7$ – 1.5 km s⁻¹). The discrepancy between the predicted LIC velocity and the measured velocity along this sight line might be an indication that the LIC velocity field is more complicated than a single vector. A similar effect has been seen toward the Hyades Cluster by Redfield & Linsky (2001), who found $v_{\text{pred}}(\text{LIC}) - v_{\text{obs}}(\text{LIC}) = 2.9 \pm 0.7$ km s⁻¹, similar to our value $v_{\text{pred}}(\text{LIC}) - v_{\text{obs}}(\text{LIC}) \sim 3.1$ km s⁻¹. The 18 Hyades stars studied by these authors are located in the sky not too far from GD 246; for four of them (HD 27561, HD 27848, HD 28237, and HD 29225; $l \sim 178^\circ$ – 184° , $b \sim -20^\circ$ to -25°), they also find $v_{\text{pred}}(\text{LIC}) - v_{\text{obs}}(\text{LIC}) \sim 3.0$ km s⁻¹.

Sulfur should not be depleted onto dust grains, making it possible to estimate how neutral hydrogen would be distributed between the two components using S II as a proxy for H I. We derive $\log N(\text{H I})_2 = 18.39$, using the S II column density for the LIC component (component 2), $\log N(\text{S II})_2 = 13.59$. We derive a distance of 8 pc to the edge of the LIC along this direction (assuming an LIC neutral hydrogen column density of $n_{\text{H I}} = 0.10$ cm⁻³; Linsky et al. 2000). Both the H I column density and the distance to the edge of the LIC derived here are greater than the values derived from the model of S. Redfield (2002, private communication) for this direction of $\log N(\text{H I}) = 17.93$ and $d = 2.75$ pc. Our values are closer to the maximum values derived for the LIC by Redfield & Linsky (2000) of 18.32 and 6.8 pc, respectively. The discrepancy between our values and the LIC model values can be due to either the prelimi-

nary nature of their model or the presence of an unresolved cloud close to the LIC velocity. While H I may not follow exactly the same distribution as S II, it is still clear that most of the neutral gas along this line of sight is outside the LIC but within the Local Bubble boundaries.

We find D I/H I = $1.51^{+0.39}_{-0.33} \times 10^{-5}$ for this line of sight (2σ error bars). So far, only three lines of sight studied by *FUSE* (HZ 43A, G191-B2B, and WD 1634–573) probing the Local Bubble have accurate D/H measurements (Kruk et al. 2002; Lemoine et al. 2002; Wood et al. 2002). This is the fourth line of sight with an accurate D/H measurement that probes the region mentioned above.

The D I/H I ratio for all the gas in this sight line is $1.51^{+0.39}_{-0.33} \times 10^{-5}$. Linsky (1998) reports a mean value of $(1.50 \pm 0.10) \times 10^{-5}$ (1σ in the mean) for 12 LIC sight lines. Because most of the gas along the sight line to GD 246 resides outside the LIC, we conclude that the D I/H I ratio for the gas outside is also $\sim 1.5 \times 10^{-5}$, similar to the LIC value.

The electron density in component 1, which probes material outside the LIC, can be computed under the assumption that electron collisions populate the upper fine-structure level ($J = 3/2$) of the ground state of C II, leading to C II* (see Spitzer & Fitzpatrick 1993). Because all the C II lines in the *FUSE* and STIS data are saturated, S II is used as a proxy for C II. This is a reasonable assumption; C II and S II have similar ionization potentials (24.38 eV for C II and 23.33 eV for S II) and should therefore trace the same type of gas. The collisional equilibrium equation is

$$A_{21}n(\text{C}^{+*}) = \gamma_{12}n_e n(\text{C}^+), \quad (1)$$

where γ_{12} is the rate coefficient for excitation and A_{21} is the spontaneous downward transition probability. For excitation of ions by electrons,

$$\gamma_{12} = \frac{8.63 \times 10^{-6}}{g_1 T^{0.5}} \Omega_{12} \exp\left(-\frac{E_{12}}{kT}\right) \text{ cm}^3 \text{ s}^{-1} \quad (2)$$

(Spitzer 1978), where $E_{12} = 7.9 \times 10^{-3}$ eV, and we adopt $A_{21} = 2.29$ (Mendoza 1983) and $\Omega_{12} = 2.90$ (Osterbrock 1989). Assuming that conditions are uniform within the cloud, we can replace particle density ratios by column density ratios, and assuming that for warm, low-density clouds the depletions of S and C are 0 and -0.3 dex, respectively,

we find

$$\frac{N(\text{C II}^*)}{N(\text{S II})} = \frac{55n_e}{T^{0.5}}. \quad (3)$$

Using the S II column density we measured for component 1, $\log N(\text{S II})_1 = 14.25 \pm 0.02$, and the C II* column density, $\log N(\text{C II}^*) = 13.05 \pm 0.04$, we find $n_e = (0.1 \pm 0.01) (T/8000)^{0.5} \text{ cm}^{-3}$ (all error bars are 2σ). For $T = 4000\text{--}8000 \text{ K}$ this yields an electron density $n_e = 0.06\text{--}0.11 \text{ cm}^{-3}$ for the material beyond the LIC, which is similar to values found in the LIC by Linsky et al. (2000).

Thus, the D/H ratio and the electron density obtained in this study indicate that the properties of the cloud(s) beyond the LIC along the GD 246 line of sight are likely similar to those of the LIC.

The presence of ionized gas in this cloud will not affect the D/H ratio in this region, as D I and H I, with similar ionization potentials, are ionized at the same rate.

Table 9 compares abundances toward GD 246 with solar photosphere abundances. We find an indication that N, O, Si, P, Ar, and Fe are depleted from typical solar abundances, but the uncertainties preclude a definitive statement. Moos et al. (2002) and Linsky (2003) have noted the evidence for 20%–25% depletion of O I by dust in the near ISM. For all species listed above, part of this depletion might be explained by not taking into account higher ionization states when calculating their gas-phase abundances. N and Si are the only species for which we could measure some of this contribution; however, we have only a lower limit on N(II), and Si III is blended with stellar Si III.

7.6. Summary

We have obtained column densities of H I, D I, C II*, N I, O I, Si II, P II, S II, Ar I, and Fe II for the line of sight to the white dwarf GD 246. This is the fourth line of sight with an accurate D/H measurement with *FUSE* that probes the region outside the LIC but inside the Local Bubble. Based on a constant D/H ratio of 1.5×10^{-5} inside the LIC, we find a similar ratio outside the LIC. In addition, our sight line-averaged D I/H I measurement for GD 246 is in agree-

TABLE 9
COMPARISON OF ABUNDANCES TOWARD GD 246 WITH
SOLAR ABUNDANCES

X	$\log(X/H)_\odot + 12$	$\log(X/H)_{\text{GD 246}}^a$	Reference
N	7.93	7.64 ± 1.30	1
O	8.69	8.56 ± 1.45	2
Si	7.54	$6.96^{+1.28}_{-1.11}$	1
P	5.51 ^b	5.18 ± 1.56	3
S	7.27 ^b	7.23 ± 1.00	3
Ar	6.40	$6.03^{+1.96}_{-1.62}$	3
Fe	7.45	6.19 ± 1.64	1

^a All uncertainties are 2σ .

^b The meteoritic and photospheric values were averaged.

REFERENCES.—(1) Holweger 2001; (2) Allende Prieto, Lambert, & Asplund 2001; (3) Grevesse & Sauval 1998.

ment with the weighted mean of D I/H I, reported by Moos et al. (2002), of $D \text{ I}/H \text{ I} = (1.52 \pm 0.08) \times 10^{-5}$ for the local ISM. For the WD 2331–475, HZ 21, and Lan 23 sight lines the column densities of D I, N I, O I, and other species are also measured and ratios are computed. We have used results from all four sight lines to compute revised *FUSE* ratios for the local ISM.

This work is based on data obtained for the Guaranteed Time Team by the NASA-CNES-CSA *FUSE* mission operated by Johns Hopkins University. Financial support to US participants has been provided in part by NASA contract NAS 5-32985 to Johns Hopkins University. Support for French participation in this study has been provided by CNES. This work is partly based on observations made with the NASA/ESA *HST*, obtained from the data archive at the Space Telescope Science Institute, which is operated by the Association of Universities for Research in Astronomy, Inc., under NASA contract NAS 5-26555. These observations are associated with proposal 7296. The PF procedure used in this work, “Owens.f,” was developed by M. Lemoine and the French *FUSE* team.

REFERENCES

- Abgrall, H., Roueff, E., Launay, F., Roncin, J. -Y., & Subtil, J.-L. 1993a, *A&AS*, 101, 273
 ———. 1993b, *A&AS*, 101, 323
 Allende Prieto, C., Lambert, D. L., & Asplund, M. 2001, *ApJ*, 556, L63
 Barstow, M. A., Dobbie, P. D., Holberg, J. B., Hubeny, I., & Lanz, T. 1997, *MNRAS*, 286, 58
 Barstow, M. A., Hubeny, I., & Holberg, J. B. 1998, *MNRAS*, 299, 520
 Chayer, P., Kruk, J. W., Vennes, S., & Dupuis, J. 2001, in *ASP Conf. Ser.* 226, 12th European Workshop on White Dwarfs, ed. J. L. Provencal, H. L. Shipman, J. MacDonald, & S. Goodchild (San Francisco: ASP), 90
 Dreizler, S., & Werner, K. 1996, *A&A*, 314, 217
 Dupuis, J., Vennes, S., & Chayer, P. 2000, *BAAS*, 197, 83.05
 Finley, D. S., Koester, D., & Basri, G. 1997, *ApJ*, 488, 375
 Friedman, S. D., et al. 2002, *ApJS*, 140, 37
 Grevesse, N., & Sauval, A. J. 1998, *Space Sci. Rev.*, 85, 161
 Hébrard, G., Mallouris, C., Ferlet, R., Koester, D., Lemoine, M., Vidal-Madjar, A., & York, D. 1999, *A&A*, 350, 643
 Hébrard, G., et al. 2001, in *XVIIth IAP Colloq., Gaseous Matter in Galaxies and Intergalactic Space*, ed. R. Ferlet, M. Lemoine, J.-M. Désert, & B. Raban (Gif-sur-Yvette: Editions Frontières), 79
 ———. 2002, *ApJS*, 140, 103
 Holweger, H. 2001, in *AIP Conf. Proc.* 598, *Solar and Galactic Composition*, ed. R. F. Wimmer-Schweingruber (New York: AIP), 23
 Howk, J. C., & Sembach, K. R. 2000, *AJ*, 119, 2481
 Jenkins, E. B., Tripp, T. M., Woźniak, P. R., Sofia, U. J., & Sonneborn, G. 1999, *ApJ*, 520, 182
 Jenkins, E. B., et al. 2000, *ApJ*, 538, L81
 Kruk, J. W., et al. 2002, *ApJS*, 140, 19
 Lallement, R., Ferlet, R., Lagrange, A. M., Lemoine, M., & Vidal-Madjar, A. 1995, *A&A*, 304, 461
 Laurent, C., Vidal-Madjar, A., & York, D. G. 1979, *ApJ*, 229, 923
 Lehner, N., Gry, C., Sembach, K. R., Hébrard, G., Chayer, P., Moos, H. W., Howk, J. C., & Désert, J.-M. 2002, *ApJS*, 140, 81
 Lemoine, M., et al. 2002, *ApJS*, 140, 67
 Levshakov, S. A., Dessauges-Zavadsky, M., D’Odorico, S., & Molaro, P. 2002, *ApJ*, 565, 696
 Lindler, D., & Bowers, C. 2000, *BAAS*, 197, 12.02
 Linsky, J. L. 1998, *Space Sci. Rev.*, 84, 285
 ———. 2003, *Space Sci. Rev.*, in press
 Linsky, J. L., Diplas, A., Wood, B. E., Brown, A., Ayres, T. R., & Savage, B. D. 1995, *ApJ*, 451, 335
 Linsky, J. L., Redfield, S., Wood, B. E., & Piskunov, N. 2000, *ApJ*, 528, 756
 Marsh, M. C., et al. 1997, *MNRAS*, 286, 369
 Mendoza, C. 1983, in *IAU Symp.* 103, *Planetary Nebulae*, ed. D. R. Flower (Dordrecht: Reidel), 143
 Meyer, D. M., Cardelli, J. A., & Sofia, U. J. 1997, *ApJ*, 490, L103
 Meyer, D. M., Jura, M., & Cardelli, J. A. 1998, *ApJ*, 493, 222
 Moos, H. W., et al. 2000, *ApJ*, 538, L1
 ———. 2002, *ApJS*, 140, 3
 Morton, D. C. 1991, *ApJS*, 77, 119
 Napiwotzki, R., Green, P. J., & Saffer, R. A. 1999, *ApJ*, 517, 399
 O’Meara, J. M., Tytler, D., Kirkman, D., Suzuki, N., Prochaska, J. X., Lubin, D., & Wolfe, A. M. 2001, *ApJ*, 552, 718
 Osterbrock, D. E. 1989, *Astrophysics of Gaseous Nebulae and Active Galactic Nuclei* (Mill Valley, CA: University Science Books)

- Pettini, M., & Bowen, D. V. 2001, *ApJ*, 560, 41
Redfield, S., & Linsky, J. L. 2000, *ApJ*, 534, 825
———. 2001, *ApJ*, 551, 413
Rogerson, J. B., Jr., & York, D. G. 1973, *ApJ*, 186, L95
Sahnou, D. J., et al. 2000, *ApJ*, 538, L7
Savage, B. D., & Sembach, K. R. 1991, *ApJ*, 379, 245
Sembach, K. R., & Savage, B. D. 1992, *ApJS*, 83, 147
Sfeir, D. M., Lallement, R., Crifo, F., & Welsh, B. Y. 1999, *A&A*, 346, 785
Sonneborn, G., Tripp, T. M., Ferlet, R., Jenkins, E. B., Sofia, U. J.,
Vidal-Madjar, A., & Woźniak, P. R. 2000, *ApJ*, 545, 277
Sonneborn, G., et al. 2002, *ApJS*, 140, 51
Spitzer, L., Jr. 1978, *Physical Processes in the Interstellar Medium* (New
York: Wiley)
Spitzer, L., Jr., & Fitzpatrick, E. L. 1993, *ApJ*, 409, 299
Vennes, S., Thejll, P. A., Galvan, R. G., & Dupuis, J. 1997, *ApJ*, 480, 714
Vidal-Madjar, A., & Ferlet, R. 2002, *ApJ*, 571, L169
Welty, D. E., & Hobbs, L. M. 2001, *ApJS*, 133, 345
Welty, D. E., Hobbs, L. M., Lauroesch, J. T., Morton, D. C., Spitzer, L., &
York, D. G. 1999, *ApJS*, 124, 465
Wolff, B., Koester, D., Dreizler, S., & Haas, S. 1998, *A&A*, 329, 1045
Wolff, B., Koester, D., & Lallement, R. 1999, *A&A*, 346, 969
Wolff, B., Kruk, J. W., Koester, D., Allard, N. F., Ferlet, R., & Vidal-
Madjar, A. 2001, *A&A*, 373, 674
Wood, B. E., Linsky, J. L., Hébrard, G., Vidal-Madjar, A., Lemoine, M.,
Moos, H. W., Sembach, K. R., & Jenkins, E. B. 2002, *ApJS*, 140, 91
York, D. G. 1983, *ApJ*, 264, 172